A closer look at the deep radio sky: Multi-component radio sources at 3 GHz VLA-COSMOS

Vardoulaki, E.; Jiménez Andrade, E. F.; Karim, A.; Novak, Mladen; Leslie, S. K.; Tisanić, Krešimir; Smolčić, Vernesa; Schinnerer, E.; Sargent, M. T.; Bondi, M.; ...

Source / Izvornik: **Astronomy and Astrophysics, 2019, 627**

Journal article, Published version
Rad u časopisu, Objavljena verzija rada (izdavačev PDF)

https://doi.org/10.1051/0004-6361/201832982

Permanent link / Trajna poveznica: https://urn.nsk.hr/urn:nbn:hr:217:267098

Rights / Prava: In copyright / Zaštićeno autorskim pravom.

Download date / Datum preuzimanja: **2024-08-17**

Repository / Repozitorij:

Repository of the Faculty of Science - University of Zagreb

A&A 627, A142 (2019)
https://doi.org/10.1051/0004-6361/201832982
© ESO 2019

Astronomy & Astrophysics

A closer look at the deep radio sky: Multi-component radio sources at 3 GHz VLA-COSMOS

E. Vardoulaki[1], E. F. Jiménez Andrade[1,2], A. Karim[1], M. Novak[3,4], S. K. Leslie[3], K. Tisanić[4], V. Smolčić[4], E. Schinnerer[3], M. T. Sargent[5], M. Bondi[6], G. Zamorani[7], B. Magnelli[1], F. Bertoldi[1], N. Herrera Ruiz[8], K. P. Mooley[9,10], J. Delhaize[4], S. T. Myers[10], S. Marchesi[11], A. M. Koekemoer[12], G. Gozaliasl[13,14,15], A. Finoguenov[14,16], E. Middleberg[8], and P. Ciliegi[7]

[1] Argelander-Institut für Astronomie, Auf dem Hügel 71, 53121 Bonn, Germany
e-mail: elenivard@gmail.com
[2] International Max Planck Research School of Astronomy and Astrophysics at the Universities of Bonn and Cologne, Germany
[3] Max-Planck-Institut für Astronomie, Königstuhl 17, 69117 Heidelberg, Germany
[4] Department of Physics, Faculty of Science, University of Zagreb, Bijenička cesta 32, 10000 Zagreb, Croatia
[5] Astronomy Centre, Department of Physics and Astronomy, University of Sussex, Brighton BN1 9QH, UK
[6] INAF – Istituto di Radioastronomia, Via Gobetti 101, 40129 Bologna, Italy
[7] INAF-Osservatorio di Astrofisica e Scienza dello Spazio di Bologna, Via Piero Gobetti 93/3, 40129 Bologna, Italy
[8] Astronomisches Institut, Ruhr-Universität Bochum, Universitätsstrasse 150, 44801 Bochum, Germany
[9] Caltech, 1200 E. California Blvd. MC 249-17, Pasadena, CA 91125, USA
[10] National Radio Astronomy Observatory, PO Box 0, Socorro, NM 87801, USA
[11] Department of Physics and Astronomy, Clemson University, Clemson, SC 29634, USA
[12] Space Telescope Science Institute, 3700 San Martin Drive, Baltimore, MD 21218, USA
[13] Finnish Centre for Astronomy with ESO (FINCA), Quantum,University of Turku, Vesilinnantie 5, 20014 Turku, Finland
[14] Department of Physics, University of Helsinki, PO Box 64, 00014 Helsinki, Finland
[15] Helsinki Institute of Physics, University of Helsinki, PO Box 64, 00014 Helsinki, Finland
[16] Max-Planck Institut für extraterrestrische Physik, Postfach 1312, 85741 Garching bei München, Germany

Received 8 March 2018 / Accepted 22 January 2019

ABSTRACT

Context. Given the unprecedented depth achieved in current large radio surveys, we are starting to probe populations of radio sources that have not been studied in the past. However, identifying and categorising these objects, differing in size, shape and physical properties, is becoming a more difficult task.
Aims. In this data paper we present and characterise the multi-component radio sources identified in the VLA-COSMOS Large Project at 3 GHz (0.75 arcsec resolution, 2.3 μJy beam^{-1} rms), i.e. the radio sources which are composed of two or more radio blobs.
Methods. The classification of objects into multi-components was done by visual inspection of 351 of the brightest and most extended blobs from a sample of 10,899 blobs identified by the automatic code BLOBCAT. For that purpose we used multi-wavelength information of the field, such as the 1.4 GHz VLA-COSMOS data and the Ultra Deep Survey with the VISTA telescope (UltraVISTA) stacked mosaic available for COSMOS.
Results. We have identified 67 multi-component radio sources at 3 GHz: 58 sources with active galactic nucleus (AGN) powered radio emission and nine star-forming galaxies. We report eight new detections that were not observed by the VLA-COSMOS Large Project at 1.4 GHz, due to the slightly larger area coverage at 3 GHz. The increased spatial resolution of 0.75 arcsec has allowed us to resolve (and isolate) multiple emission peaks of 28 extended radio sources not identified in the 1.4 GHz VLA-COSMOS map. We report the multi-frequency flux densities (324 MHz, 325 MHz, 1.4 GHz & 3 GHz), star formation rates, and stellar masses of these objects. We find that multi-component objects at 3 GHz VLA-COSMOS inhabit mainly massive galaxies ($>10^{10.5}$ $M_{\odot}$). The majority of the multi-component AGN lie below the main sequence of star-forming galaxies (SFGs), in the green valley and the quiescent region. Furthermore, we provide detailed descriptions of the objects and find that amongst the AGN there are two head-tail, ten core-lobe, nine wide-angle-tail (WAT), eight double-double or Z-/X-shaped, three bent-tail radio sources, and 26 symmetric sources, while amongst the SFGs we find the only star-forming ring seen in radio emission in COSMOS. Additionally, we report a large number (32 out of 58) of disturbed/bent multi-component AGN, 18 of which do not lie within X-ray groups in COSMOS (redshift range $0.08 \leq z < 1.53$).
Conclusion. The high angular resolution and sensitivity of the 3 GHz VLA-COSMOS data set give us the opportunity to identify peculiar radio structures and sub-structures of multi-component objects, and relate them to physical phenomena such as AGN or star-forming galaxies. This study illustrates the complexity of the μJy radio-source population; at the sensitivity and resolution of 3 GHz VLA-COSMOS, the radio structures of AGN and SFG both emitting radio continuum emission, become comparable in the absence of clear, symmetrical jets. Thus, disentangling the AGN and SFG contributions using solely radio observations can be misleading in a number of cases. This has implications for future surveys, such as those done by square kilometre array (SKA) and precursors, which will identify hundreds of thousands of multi-component objects.

Key words. catalogs – galaxies: active – galaxies: star formation – radio continuum: galaxies

1. Introduction

For several decades astronomers have been exploring the radio part of the electromagnetic spectrum, probing the physical phenomena that are responsible for emitting at radio wavelengths (see Simpson 2017, for a review). Thanks to the greater sensitivity of modern radio observatories such as the Karl G. Jansky Very Large Array (VLA), we now have the opportunity to study in greater detail and depth populations of objects. Radio observations, being dust-free probes of star formation (SF), pinpoint the birthplace of stars within galaxies and can also highlight the complexity of radio structures emitted by active galactic nuclei (AGN). They further aid the study of feedback mechanisms from AGN (e.g. De Young 2010; Best et al. 2014; Williams & Röttgering 2015). Radio observations, in combination with multi-wavelength observations are a powerful tool to study the physical processes behind the formation of the stars in galaxies, as well as the energy released by AGN in their environment in the form of kinetic energy, probed by synchrotron radiation (e.g. Willott et al. 1999; Smolčić et al. 2017a).

For galaxies, the radio-frequency range below 10 GHz is dominated by non-thermal synchrotron radiation (e.g. Condon 1992). As a result, radio studies in this range pick up populations of radio sources that are either powered by AGN or SF, as both physical phenomena emit non-thermal synchrotron radiation. Additionally, in some cases both phenomena simultaneously occur (hybrid or composite objects, for example Symeonidis et al. (2013), Seymour et al. (2009), but see Padovani (2016) for a different point of view on the nomenclature of these hybrid objects). In the case of star formation, in the radio we observe synchrotron radiation from cosmic-ray electrons accelerated by supernova remnants (e.g. Condon 1992; Murphy 2009), such that non-thermal radio emission traces the most recent episodes of massive star-formation. In the case of AGN, synchrotron radiation that is observed at radio wavelengths originates from relativistic electrons spiralling around the magnetic field associated with the central black hole region (see Antonucci 1993; Netzer 2015, for a review of unified AGN models). The so-called radio-mode feedback (e.g. Fabian 2012) from AGN, or kinetic/jet feedback, which is thought to prevent massive galaxies in the present-day Universe from carrying out new star formation activities (e.g. Ishibashi et al. 2014), can have different observational signatures in the radio, giving rise to complex radio structures.

Traditionally, radio AGN with extended radio structures are classified as edge-brightened or FRII (lobe-like radio sources) and as edge-darkened or FRI (jet-like radio sources) depending on the distribution of power along their radio structure (Fanaroff & Riley 1974). Thus in large radio surveys one can find radio sources of different types, shapes, and sizes, some single-component and some composed of several components (or multi-component; e.g. lobes, jets, star-forming regions). These systems can exhibit peculiar and complex structures, which gives rise to questions regarding their formation and their interaction with the surrounding intergalactic (IGM) and/or intra-cluster medium (ICM). The complexity of the structures observed in radio surveys, as well as the different sizes and shapes, in combination with the two physical phenomena in place (AGN or SF), hold a challenge when it comes to current automatic identification and classification algorithms (e.g. BLOBCAT, PYBDSF; Hales et al. 2012; Mohan & Rafferty 2015, respectively). These algorithms cannot fully undertake the task of identifying multiple components, and disentangling AGN and SF objects through their radio signatures.

Here we present the multi-component radio sources in the VLA-COSMOS Large Project at 3 GHz (Smolčić et al. 2017c), and compare them to their 1.4 GHz analogues presented by Schinnerer et al. (2007, 2010). We discuss the difficulties of identifying multi-component radio sources in radio mosaics given the complexity and plethora of the radio structures found at such low flux densities, ranging from 100 μJy down to ~10 μJy. We present a value added catalogue for these objects with corrected radio positions and core flux densities, as well as radio properties and properties of the host, such as star formation Sect.rate (SFR) and stellar mass (M_*), in Sect. 2. We also create a tool (presented in Appendix C) to cross-match multi-component sources to their analogues at other radio frequencies in COSMOS, by taking into account the different angular resolution of those surveys and the size of our objects. We present an analysis on the SFR and stellar masses of their host galaxies in Sect. 3.1. Furthermore we provide some general notes on the objects (Sect. 3.2), while a more detailed description based on their radio structure can be found in Appendix D. We close our paper with a discussion on the need for automatic identification methods that can identify multi-component sources and disentangle AGN and SF objects (Sect. 4). The objects presented here are shown in Fig. D.7 in the Appendix.

Throughout this paper we use the following convention for all spectral indices, α: flux density is $S_\nu \propto \nu^{-\alpha}$, where ν is the observing frequency. Also, a low-density, Λ-dominated Universe in which $H_0 = 70\,\mathrm{km\,s^{-1}\,Mpc^{-1}}$, $\Omega_\mathrm{M} = 0.3$, and $\Omega_\Lambda = 0.7$ is assumed throughout. For the estimation of star formation rates and stellar masses, a Chabrier (2003) initial mass function (IMF) was used.

2. Analysis of multi-component sample

In this paper we present the multi-component radio sources from the VLA-COSMOS Large Project at 3 GHz (Smolčić et al. 2017c, 3 GHz VLA-COSMOS henceforth), that is, objects that are composed of two or more radio blobs, or islands of pixels representing sources. The survey is complete down to 40 μJy (94%; see Fig. 16 of Smolčić et al. 2017c) at a resolution of 0.75 arcsec and rms of 2.3 μJy beam^{-1}. Details on the data reduction can be found in Smolčić et al. (2017c).

In the radio mosaic, radio emission of some morphologically complex galaxies can be split into multiple blobs if the surface brightness drops below the detection threshold. For example, this might happen when the radio emission is composed of a core, faint jets and bright lobes, or several disjointed star-forming regions. Given the sub-arcsec resolution of the 3 GHz data we expect that individual components of such sources are extended with non-Gaussian structures.

We note that the definition of multi-component sources in this paper differs from other definitions that deem multi-component sources those made up by multiple Gaussian components (e.g. Schinnerer et al. 2007). Our definition of multi-component, as in Smolčić et al. (2017c), has to do with a parent source being composed of two or more islands/blobs.

For the identification and classification of the objects we make use of the 1.4 GHz VLA-COSMOS Large Project (Schinnerer et al. 2007, 2010), which surveyed the 2 deg^2 of the COSMOS field at a resolution of ~1.5 arcsec. We also make use of the optical/near-infrared stacked $YJHK_s$ image from the Ultra Deep Survey with the Visible and Infrared Survey Telescope for Astronomy (VISTA) (UltraVISTA; see Laigle et al. 2016; Smolčić et al. 2017b, and references therein), including regions observed at z^{++} with an upgrade of the Subaru Suprime-Cam (see Taniguchi et al. 2007, 2015; Smolčić et al. 2017b). Laigle et al. (2016) combined the near-IR images of UltraVISTA ($YJHKs$) with the optical z^{++}-band data from Subaru in order to probe

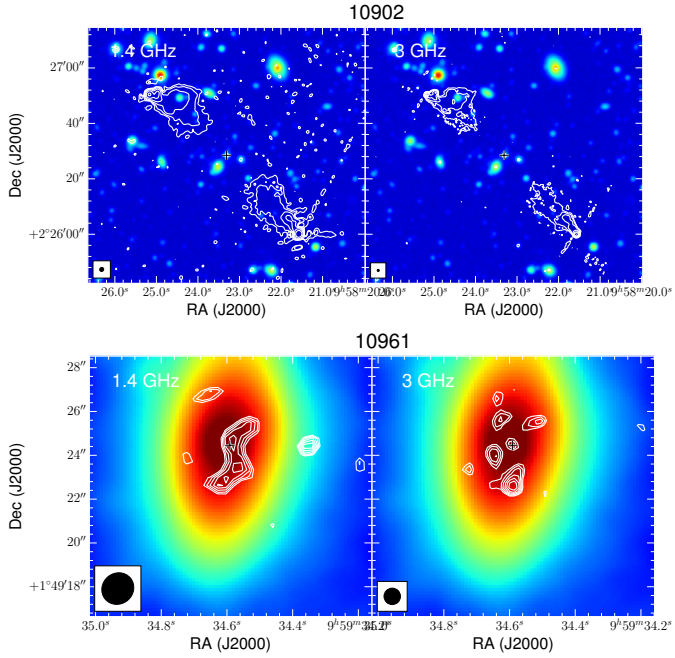

Fig. 1. Set of 1.4 GHz VLA (*left*) and 3 GHz VLA (*right*) stamps for two of the radio multi-component objects in the COSMOS field shown as white contours, overlaid on the UltraVISTA stacked image shown in colour scale in arbitrary units. The beam size for the radio observations is at the bottom left corner of the stamp: 1.4×1.5 arcsec^2 for the 1.4 GHz and 0.75 arcsec FWHM for the 3 GHz maps. The black cross denotes the 3 GHz radio position as in Table A.1. The contour levels are equally spaced on a log scale, where the lowest is set at 3σ and the highest at the maximum peak flux density of the radio structure. The top set of stamps shows an example of radio AGN, while the bottom set shows a SFG. The remainder of the maps can be found throughout the text, grouped in categories depending on the type of the object and in the Appendix.

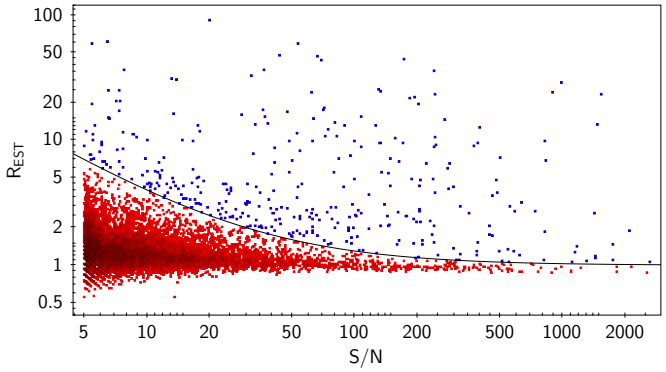

Fig. 2. R_{EST} parameter (a size estimate from BLOBCAT not intended for quantitative analysis; Hales et al. 2012) versus signal-to-noise ratio (S/N) for the 10899 entries in the BLOBCAT catalogue identified from the 3 GHz mosaic of the COSMOS field. The black solid line separates the sources that obey the relation $R_{EST} > 1 + 30/(S/N)$ and were visually inspected to create the multi-component sample from the rest of the 3 GHz sources, as described in Sect. 2.1.

the high-redshift Universe and provide a catalogue containing UV-luminous sources at $z > 2$. The photometry was done using SExtractor in dual image mode and the stacked image created using SWARP (Bertin et al. 2002). The final product is a stacked image at $z^{++}YJHK_s$, which we will refer to from now on as UltraVISTA stacked or χ^2 map, and has arbitrary units. This map helped significantly in identifying which blobs belong to which source, as is described further down. Without the use of multi-wavelength data, a solely radio-based classification is not conclusive (see Sect. 4.3 for an example).

2.1. Source identification and matching of radio blobs

To identify sources in the 3 GHz mosaic, Smolčić et al. (2017c) used the automatic algorithm BLOBCAT (Hales et al. 2012), which locates islands, or radio blobs, assigns a catalogue number or ID, and performs flux density, rms, position, and size measurements amongst others. This and similar codes (e.g. PYBDSF; Mohan & Rafferty 2015) perform well for single source identification. Nevertheless, to date, even the very advanced codes available (see Fan et al. 2015, for a bayesian approach) cannot completely substitute the time-consuming step of visual inspection. For that reason visual inspection of the sample is required, and not only as a validation test. BLOBCAT produced a catalogue from the 3 GHz mosaic with 10899 entries, which makes it time consuming to visually inspect all radio blobs. Furthermore, as the visual inspection technique is quite subjective depending on the inspector and their knowledge of the physics of these objects, the exercise will need to be repeated independently by several inspectors to get to a reliable match.

To limit the number of components that require visual inspection, and to pick up objects composed of several radio blobs (e.g. lobes from an AGN that extend beyond the host galaxy), we utilise the R_{EST} parameter reported by BLOBCAT. This parameter provides a size estimate in the units of the sky area covered by an unresolved Gaussian blob with the same peak surface brightness (see Eq. (34) in Hales et al. 2012). The larger the value ($R_{EST} > 1.4$; suited for automatically flagging complex blobs), the more likely the source has a complex radio structure, while the value of one corresponds to a point source. Random noise variations can also contribute to the size estimate, especially at low signal-to-noise ratios (S/N). For this reason, we have chosen by eye an envelope defined as $R_{EST} > 1 + 30 \times (S/N)^{-1}$ (shown in Fig. 2 as black line) to select likely candidates for complex sources. Such a selection yields 351 components in total, shown in blue, which is a fairly small number of blobs on which to perform visual inspection on. These components were then combined into multi-component sources where necessary (see also Sect. 3.3 in Smolčić et al. 2017c). To make sure we do not miss FR-type multi-component objects due to our selection, the entire 2.6 deg^2 mosaic was visually inspected, despite this being highly impractical and time consuming.

Within these sources there are 127 known and previously observed extended radio AGN from the VLA-COSMOS survey at 1.4 GHz (Schinnerer et al. 2007, 2010), which aided in the matching process[1]. The R_{EST} envelope was selected to pick up the brightest and most extended radio components. Less bright components that might be part of the parent source and fall below the envelope in Fig. 2 are picked up as components of the parent radio source after visual inspection.

In this paper we go beyond a radio-only classification, in order to avoid mismatches and mis-classifications. Thus we created overlays of the radio 3 GHz and the stacked UltraVISTA map, similar to what is presented in Figs. 1 and D.7. The maps

[1] At the resolution of the 1.4 GHz observations (1.5 arcsec), their analogues are not necessarily multi-component objects (see Fig D.7), as their radio structure might not be divided into several radio blobs. The reason for this is partly the different and coarser resolution than at 3 GHz and partly due to diffuse emission being missed at 3 GHz.

were inspected visually by seven researchers of the group to match the radio blobs to the corresponding optical/near-IR counterpart. At a later stage, Smolčić et al. (2017b) performed counterpart association, that is they combined the 3 GHz radio data with optical, near-infrared (UltraVISTA; see Laigle et al. 2016, and references therein), and mid-infrared Spitzer infrared array camera (IRAC) data (Sanders et al. 2007), as well as X-ray data (*Chandra*-COSMOS and COSMOS-Legacy; Elvis et al. 2009; Civano et al. 2012, 2016; Marchesi et al. 2016), to match the radio sources to their corresponding hosts out to $z < 6$. In this procedure, they made use of the latest photometric catalogue available for COSMOS (henceforth COSMOS2015; Laigle et al. 2016). For the multi-component objects, the locations of the hosts were re-examined by eye. There is only one mismatch with the counterpart catalogue, that of source ID 10904, where the radio position was given between two neighbouring galaxies. Thus we re-measured the radio position and we present it in Table A.1.

After carefully inspecting and matching the blobs to single radio sources, we re-measured the radio positions and flux densities, as well as local rms and added the matched sources as new entries in the VLA catalogue produced by BLOBCAT after removing multiple entries. The matched components, deemed multi-component radio sources at 3 GHz VLA-COSMOS, were assigned a new ID starting from 10900 to 10966. The full sample of multi-component radio sources is presented in Table A.1.

Furthermore, objects were classified as AGN or SFGs based on their characteristic radio structure with the aid of the 1.4 GHz maps and the UltraVISTA χ^2 map, which highlights the location of the host galaxy, in the following way:

1. AGN: Multi-component sources with two or more blobs that belong to the same parent radio source and resemble jets or lobes produced by an AGN.
2. SFGs: Multi-component sources composed of several blobs that are associated with the disk of the galaxy in the optical/near-IR, and they do not resemble jets/lobes produced by an AGN.

In Fig. 1 we give examples of the two main categories of objects, AGN (top; 10902) and star-forming galaxies (SFGs; bottom; 10961), presented in this paper. The rest of the objects can be found in the Appendix in Fig. D.7. For comparison, we also present the 1.4 GHz maps for each multi-component source, overlaid as contours on the UltraVISTA stacked image.

The total flux of the multi-component sources was derived in the following way. Firstly, a more reliable determination of the noise close to bright and extended sources was derived measuring the rms of the total intensity image in a region at least 200×200 pixels^2 nearby the radio source but free of radio emission. Then the image was blanked down to two times the rms and the total flux density was measured using the AIPS task TVSTAT that allowed for the integration of the multi-component source flux density over irregular areas. Secondly, we measured the core flux densities of AGN-type multi-component objects by fitting a Gaussian component around the radio core using the task IMFIT in common astronomy software applications (CASA) (McMullin et al. 2007). When needed, radio positions were corrected to match that of the core, as the BLOBCAT algorithm provides the position of the weighted mean, which in this case does not correspond to the core position. All values and radio positions are presented in Table A.1, along with redshift information and the 1.4 GHz analogue. Finally, we provide information about the corresponding very long baseline array (VLBA) source from Herrera Ruiz et al. (2017).

In Fig. 3-Top we compare the radio luminosities of the multi-component radio sources at 3 GHz to the rest of the objects at

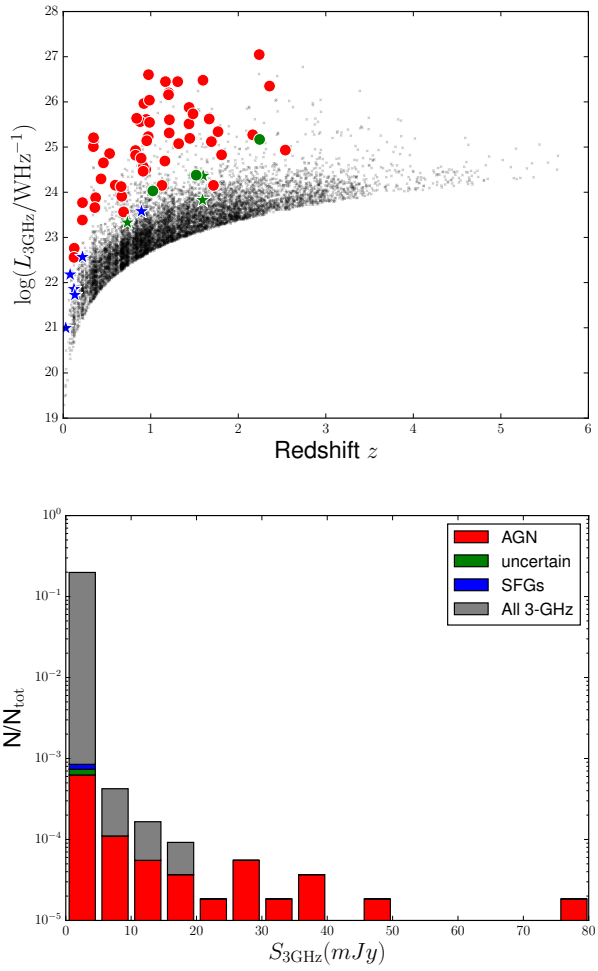

Fig. 3. *Top*: radio luminosity at 3 GHz versus redshift showing the multi-component radio sources compared to the single-component radio sources at 3 GHz. Symbols: red circles are multi-component AGN; blue stars are multi-component SFGs; green circles/stars are for uncertain class, where a circle is for AGN and a star for SFG based on the radio excess (see Sect. 3.1); small black crosses show the single-component radio sources at 3 GHz. *Bottom*: flux density histogram showing the multi-component objects (AGN in red, uncertain in green and SFGs in blue) relative to the full 3 GHz sample (grey).

3 GHz COSMOS which are single-component radio sources. We see that multi-component objects occupy the region in the L–z diagram of higher luminosities rather than the single-component objects at the corresponding redshifts. This can be seen more clearly in the flux density histogram in Fig. 3-Bottom, where at flux densities above 20 mJy we only find AGN multi-component objects.

Furthermore, in Table 1 we give the host properties of the multi-component radio sources, such as SFR and stellar mass, from the counterpart catalogue of Smolčić et al. (2017b), and the COSMOS2015 identification number. We also provide classification, AGN or not, based on the spectral energy distribution (SED) fit (Delvecchio et al. 2017; Smolčić et al. 2017b).

The SFR and M_* used in this analysis were obtained from the study of Delvecchio et al. (2017), after fitting the multi-wavelength SEDs of these objects with the SED-fitting code MAGPHYS (da Cunha et al. 2008) and the three-component SED-fitting code SED3FIT by Berta et al. (2013), which accounts for an additional AGN component. In particular they use the plethora of data in the COSMOS2015 catalogue (Laigle et al. 2016),

Table 1. Multi-component host properties.

3 GHz ID	SFR_{IR} ($M_\odot\,yr^{-1}$)	$\log_{10}(M_*)$ ($M_\odot$)	SED AGN	Radio Class	COSMOS 2015
(1)	(2)	(3)	(4)	(5)	(6)
10900	56.29	11.47	T	AGN-WAT	934339
10901	329.01	11.32	F	AGN-SYM	446143
10902	30.51	10.61	T	AGN-SYM	754369
10903	29.25	11.01	T	AGN-CL	912632
10904	91.75	9.84	T	AGN-SYM	458870
10905	6.92	11.46	F	AGN-SYM	809167
10906	11.57	11.11	F	AGN-SYM	809443
10907	16.05	11.21	F	AGN-SYM	761486
10908	–	–	F	AGN-SYM	380833
10909	125.21	11.63	F	AGN-XZ	936454
10910	5.59	11.30	F	AGN-WAT	350495
10911	32.35	11.49	T	AGN-SYM	486067
10912	5.63	11.46	F	AGN-CL	636013
10913	4.29	11.67	F	AGN-WAT	901584
10914	9.94	11.12	F	AGN-XZ	561934
10915	174.84	11.10	F	AGN-XZ	343802
10916	8.37	10.90	F	AGN-SYM	374634
10917	24.96	11.34	F	AGN-BT	960761
10918	1.19	11.59	F	AGN-XZ	996897
10919	37.50	11.00	F	AGN-XZ	407780
10920	76.76	10.76	F	AGN-SYM	210704
10921	11.92	10.83	F	AGN-SYM	759401
10922	5.92	11.43	F	AGN-SYM	1349607
10923	26.74	11.63	F	AGN-SYM	333779
10924	–	–	F	AGN-CL	351323
10925	11.31	11.21	F	AGN-SYM	372940
10926	34.08	10.89	F	AGN-SYM	429082
10927	7.00	10.66	F	AGN-CL	517689
10928	14.10	10.86	F	AGN-SYM	978441
10929	49.87	10.92	F	AGN-CL	410131
10930	96.83	11.41	F	AGN-SYM	374873
10931	4.23	11.39	F	AGN-WAT	292852
10932	24.92	9.18	F	AGN-SYM	345618
10933	2.48	11.53	F	AGN-XZ	305535
10934	5.34	11.21	F	AGN-SYM	570506
10935	35.67	11.33	F	AGN-XZ	873867
10936	4.46	11.01	F	AGN-SYM	202465
10937	17.63	11.07	F	AGN-SYM	575428
10938	–	–	F	AGN-SYM	351652
10939	83.56	11.64	T	AGN*-CL	195117
10940	34.55	10.39	T	AGN*-CL	609017
10941	90.12	11.06	F	AGN*-CL	134089
10942	7.06	11.03	F	SFG*	323222
10943	0.80	8.10	F	AGN-CL	163557
10944	4.89	11.45	F	SFG	869036
10945	2.45	11.22	T	AGN-CL	801950
10946	38.98	11.53	F	SFG	1124349
10947	251.99	10.51	F	AGN-BT	261526
10948	0.44	11.28	F	AGN-SYM	447542
10949	7.82	11.40	F	AGN-WAT	1003852
10950	0.20	10.75	F	AGN-WAT	1068567
10951	140.78	11.72	F	AGN-SYM	565211
10952	4.99	11.00	F	AGN-WAT	704802
10953	3.91	11.30	F	AGN-SYM	826044
10954	1.93	9.67	F	SFG	955856

Notes. Host-galaxy properties. Column 1: 3 GHz VLA-COSMOS ID; Columns 2 and 3: SFR calculated from the IR SED in $M_\odot\,yr^{-1}$ and logarithm of the stellar mass M_* in $M_\odot$ from the SED fit from Delvecchio et al. (2017), respectively; Column 4: AGN based on the SED fit (Delvecchio et al. 2017) or not ("T" for AGN, "F" no AGN); Column 5: radio class as in Table A.1 also presented here as a visual aid to the reader; Column 6: COSMOS2015 ID from Laigle et al. (2016) and counterpart catalogue in Smolčić et al. (2017b).

Table 1. continued.

3 GHz ID	SFR_{IR} ($M_\odot\,yr^{-1}$)	$\log_{10}(M_*)$ ($M_\odot$)	SED AGN	Radio Class	COSMOS 2015
(1)	(2)	(3)	(4)	(5)	(6)
10955	1.65	10.62	F	AGN-HT	869175
10956	0.72	11.20	F	AGN-WAT	689074
10957	4.23	11.10	F	AGN-HT	544105
10958	0.24	11.08	F	AGN-XZ	744655
10959	33.94	11.37	F	AGN-SYM	957772
10960	4.75	10.70	F	SFG	657397
10961	4.03	10.76	F	SFG	342091
10962	32.10	10.95	T	AGN-WAT	931677
10963	596.79	10.38	F	SFG*	902320
10964	188.52	12.12	T	SFG*	223951
10965	11.03	11.35	F	SFG	234240
10966	1.25	11.04	F	AGN-BT	182559

including Herschel observations to constrain the far-infrared part of the SED for lower redshift galaxies, while for higher redshift they include a large dataset of sub-millimetre (sub-mm) photometry from JCMT/SCUBA-2, LABOCA, Bolocam, JCMT/AzTEC, MAMBO, ALMA, and PdBI (see Sect. 2.2 in Delvecchio et al. 2017, for references and discussion). In addition they make use of the *Chandra*-COSMOS (Elvis et al. 2009; Civano et al. 2012) and COSMOS-Legacy (Civano et al. 2016) X-ray catalogues.

2.2. Multi-frequency radio data

In Table 2 we present radio photometry from MHz to GHz frequencies for the multi-component objects at 3 GHz. We have matched the 3 GHz radio positions to the following radio catalogues: 324 MHz from VLA (Smolčić et al. 2014); 325 MHz from the Giant Metrewave Radio Telescope (GMRT; Tisanić et al. 2019); and 1.4 GHz from VLA (Schinnerer et al. 2010). The matching of the multi-frequency data with the 3 GHz multi-component sources was done by an automatic code, which is described in Appendix C. In short, the code takes as prior the positions of the 3 GHz multi-component objects and searches within the area covered by the source, rejecting near-by objects that are not associated with it. The area covered by the source at 3 GHz was estimated by the linear-projected size of the source, which was measured using a semi-automatic method presented in Vardoulaki et al. (in prep.). In some cases more than one blob was matched to a 3 GHz radio source. We thus report in Table 2 the multi-frequency flux densities and whether the source is a multi-component or not at the corresponding radio frequency. In the following paragraphs, we briefly describe the aforementioned radio surveys.

The 324 MHz mosaic (Smolčić et al. 2014) is a shallow survey of the COSMOS field, covering 3.14 deg^2, with an average rms noise level of 0.5 mJy $beam^{-1}$ and an angular resolution of $8\farcs0 \times 6\farcs0$. The extracted catalogue includes 182 sources (down to 5.5σ). Details on the observations can be found in Smolčić et al. (2014).

The GMRT radio map at 325 MHz is the result of a single pointing covering the ∼2 deg^2 of the COSMOS field. This was observed for 45 hrs under the project 07SCB01 (P.I.: S. Croft). The 325 MHz catalogue were created from the GMRT maps (Tisanić et al. 2019) using BLOBCAT down to a 5σ limit, giving 633 radio blobs. At 325 MHz the angular resolution is $\sim 10\farcs8 \times 9\farcs5$ with a median rms of 87 μJy $beam^{-1}$.

Table 2. Multi-frequency flux densities.

3 GHz	S (mJy)			
ID	324	325	1.4	3
	(MHz)		(GHz)	
(1)	(2)	(3)	(4)	(5)
10900	155.1	131.9	60.51	35.17
10901	260.3	233.9	53.03	18.16
10902	472.1	421.5	116.5	46.16
10903	17.81	16.41	10.61^{2m}	6.950
10904	205.1	182.4	64.60^{2m}	28.42
10905	12.40	10.43	5.673	3.170
10906	60.33	54.33	19.21	8.651
10907	10.90	8.862	5.271	2.814
10908	156.3	–	–	26.23
10909	32.73	30.50	12.99^{2m}	6.828
10910	–	30.36	15.10	5.867
10911	3.008	16.27	7.509	3.425
10912	–	2.777	2.200^{2m}	1.220
10913	172.8	207.6	82.83^{2m}	32.09
10914	21.62	19.17	7.751	3.327
10915	46.97	42.07	9.799	3.692
10916	32.74	34.66	12.92^{2m}	5.438
10917	6.394	7.087	2.658	1.523
10918	114.0	136.4	57.26^{2m}	25.22
10919	24.60	26.16	8.119	3.157
10920	15.73	18.09	4.706	1.975
10921	–	4.486	2.422	0.981
10922	237.4	–	–	24.15
10923	143.5	135.1^{2m}	37.02	13.17
10924	–	–	–	9.353
10925	146.0	144.7	47.23	18.54
10926	9.163	9.158	2.027	0.744
10927	9.929	–	3.428	1.055
10928	88.64	93.43	30.12	11.64
10929	–	–	0.675^{2m}	0.298
10930	–	3.603	1.173	0.578
10931	–	4.458	2.275	0.867
10932	–	–	–	0.816
10933	227.4	217.2	88.17	39.30
10934	–	–	0.942	0.380
10935	15.56	20.19	6.548	2.382
10936	101.3	82.80	29.13	10.05
10937	–	1.122	0.432	0.230
10938	–	–	–	0.849
10939	–	3.601	0.920^{2m}	0.367
10940	–	0.998	0.411	0.204
10941	–	–	–	0.549
10942	–	–	0.107	0.374
10943	–	4.925	0.994^{2m}	0.406
10944	–	6.033	2.815	0.948
10945	–	–	–	0.205
10946	–	–	–	0.116
10947	–	0.944	0.313	0.120

Notes. Multi-frequency analogues to the 3 GHz multi-component radio sources. Data: 324 MHz from VLA (Smolčić et al. 2014); 325 MHz from GMRT (Tisanić et al. 2019); 1.4 GHz from VLA (Schinnerer et al. 2007); and 3 GHz from VLA (Smolčić et al. 2017c). The character m denotes the source is multi-component at the corresponding radio frequency, and that the flux densities of the individual components have been added together giving the value presented here; the number in front of it denotes the number of blobs added together.

Table 2. continued.

3 GHz	S (mJy)			
ID	324	325	1.4	3
	(MHz)		(GHz)	
(1)	(2)	(3)	(4)	(5)
10948	–	2.982	2.625	1.943
10949	7.472	6.975	5.422	2.718
10950	3.242	–	–	1.439
10951	–	2.286	1.827^{2m}	0.890
10952	–	8.662	4.533	1.687
10953	–	6.276	3.192	1.254
10954	–	2.306	1.387	0.508
10955	–	4.636	6.229	1.058
10956	–	24.98	17.04^{3m}	4.379
10957	–	3.933	1.774	0.514
10958	–	4.354	2.305	0.889
10959	158.3	144.1	35.14^{2m}	8.576
10960	–	–	0.595	0.188
10961	–	–	0.334	0.107
10962	682.6	571.9	175.5	80.25
10963	–	–	0.302	0.152
10964	–	–	0.102	0.092
10965	–	–	0.526	0.263
10966	–	6.403	2.873	0.861

A comparison between 324 and 325 MHz shows a non-negligible difference between the values, which points to the difficulty of measuring homogeneous flux densities for these sources. In Table 2 we see that the majority of multi-component sources 98% are single-component sources at 325 MHz, which is a result of the much lower resolution compared to the 3 GHz (10″ arcsec).

The 2 deg^2 of the COSMOS field were observed by Schinnerer et al. (2007) at 1.4 GHz with the VLA, reaching the angular resolution of 1.″5 × 1.″4 and a mean rms of 10.5 (15) μJy beam in the central 1 (2) deg^2, yielding ∼3600 radio sources. From the 67 multi-component radio sources in the 3 GHz VLA-COSMOS map, 28 objects are not classified as such at 1.4 GHz, instead they are single-component radio sources. This number is derived by visual inspecting the 1.4 GHz cutouts. Thus at 3 GHz we find ∼42% more multi-component sources than at 1.4 GHz. This is due to the higher resolution of 0.75 arcsec at 3 GHz, compared to 1.5 arcsec at 1.4 GHz. As a result, diffuse radio emission seen at 1.4 GHz might be resolved out, and the observational consequence is that the radio flux distribution splits into several components. In fact, we find that, on average, flux densities at 1.4 GHz are by ∼30% larger than the ones expected on the basis of the 3 GHz flux densities, assuming a simplistic radio spectral index of 0.8. This suggests that at 3 GHz we are missing part of the diffuse emission seen at 1.4 GHz. Furthermore, we find 8 new identifications at the edges of the 3 GHz mosaic (2.6 deg^2), which were not recovered by the 2 deg^2 1.4 GHz observations (10908, 10922, 10924, 10932, 10938, 10941, 10946 and 10950). In Appendix B we test how the coarser resolution can change the appearance of the 3 GHz multi-component sources. We note that our classification of multi-component sources differs from the one in Schinnerer et al. (2007, 2010), where they deem multi-component objects those that can be fit by multiple Gaussians, thus we refrain from adding their classification in Table 2. Instead we only present the results from matching the 1.4 and 3 GHz data with the matching method described in Appendix C.

3. A closer look at the multi-component objects

As explained in Sect. 2.1, we classified objects as AGN if they have clear signs of jets or lobes, and as SFGs if they show other characteristics where the radio emission follows the optical/near-IR morphology. The multi-component VLA-COSMOS radio sources at 3 GHz are either AGN (58 out of 67 objects) or star-forming galaxies (nine out of 67). We note that six of the 67 objects have uncertain classification on the basis of their radio structure, and they are placed on the AGN or the SFG class using a radio AGN diagnostic from Delvecchio et al. (2017) (see Sect. 3.1). Multi-component AGN exhibit radio lobes and jets, which in most cases extend out to large distances from the host galaxy (e.g. 10900, 10913, 10918). Multi-component SFGs are composed of several radio blobs associated with star-forming regions (10944, 10946, 10954, 10960, 10961, 10965; see Fig. D.5). Some of the AGN show peculiar radio structure due to strong interaction with the environment or due to internal physical mechanisms (see Sect. 3.2 and Appendix D).

Out the 58 objects with a 1.4 GHz detection, 28 are not multi-component radio sources at 1.4 GHz due to the coarser resolution of 1.5 arcsec (see Fig. D.7 in the Appendix). An example is 10966 (see Fig. D.4), where the lobes are separated at 3 GHz but not at 1.4 GHz. Two other examples are 10960 and 10944 (see Fig. D.5), which exhibit at least two radio blobs at 3 GHz associated with the host galaxy disc, almost forming a ring around the nucleus; this is not seen at 1.4 GHz where the emission comes from the whole galaxy disc. Additionally, the 3 GHz data reveal in higher detail the sub-structure in the jets of radio AGN (e.g. 10910, 10913, and 10956 in Fig. D.2, and 10918 in Fig. D.3).

There are objects that do not appear completely separated at 3 GHz (e.g. 10933, 10962; Figs. D.3 and D.2, respectively) but are included in the multi-component catalogue due to the way BLOBCAT identifies blobs. If the surface brightness falls below 2.5σ, then it separates the source into different islands. Sources 10933 and 10962 have small components near the main source associated with them, so to include them in the total flux density measurements we had to re-measure their flux densities.

In the following sub-sections we present an analysis on the hosts of the multi-component objects in our sample (Sect. 3.1), as well as some brief notes on the objects (Sect. 3.2), with a more detailed description in Appendix D.

3.1. Hosts of 3 GHz multi-components

To further investigate the nature of the radio emission from the 67 multi-component objects, we use their SFR and M_* quantities derived by Delvecchio et al. (2017) to explore their offset with respect to the main sequence (MS) of SFGs from Whitaker et al. (2012), defined as ΔsSFR–M_*. In Fig. 5 we plot the logarithmic difference between the specific star formation rate (sSFR) and the specific star formation rate of objects on the main sequence of star forming galaxies ($\mathrm{sSFR_{MS}}$) versus stellar mass M_* diagram, and infer trends regarding the hosts of the multi-component objects.

As seen in Fig. 5, the six multi-component SFGs at 3 GHz lie within the 1σ dispersion of the MS, while the multi-component AGN have hosts that are spread around the diagram, with some objects lying below the MS and some within the MS. The AGN hosts are mainly massive galaxies with masses above $10^{10.5}\,M_\odot$, with the exception of 10904, 10932 and 10943. The latter object seems to have been assigned a counterpart in the Smolčić et al. (2017b) catalogue that does not actually match to the core of the 3 GHz radio source (see Fig. D.7). Instead it matches to the western lobe of the source. We flag this identification as uncertain (see Fig. D.7). Regarding the SFGs (Fig. D.5), their hosts have masses above $10^{9.5}\,M_*$. Also, from their radio structure we do not have any indication that their radio emission is powered by an AGN. The multi-wavelength data available for COSMOS support that these are star-forming objects (see also Table 1).

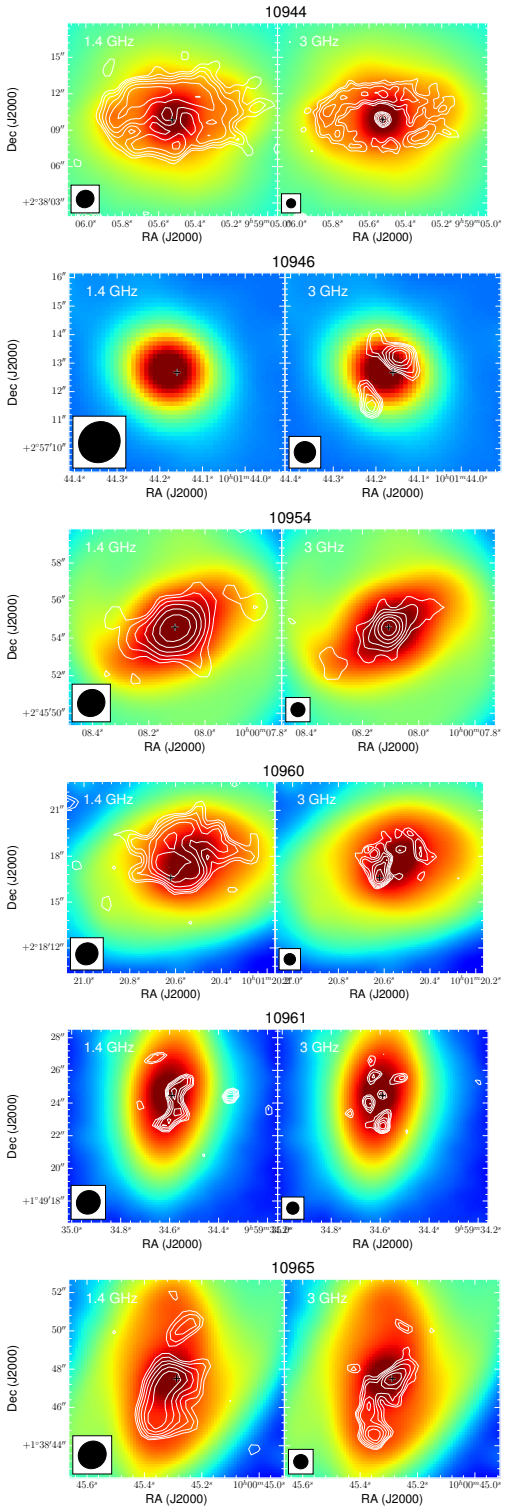

Fig. 4. The six star-forming galaxies in our multi-component radio sample at 3 GHz. Images are described in Fig. 1.

Multi-component objects with uncertain radio classification, that is objects without clear signs of jets (10939, 10940, 10941, 10942, 10963, 10964; Fig. 6), are mainly located on the MS,

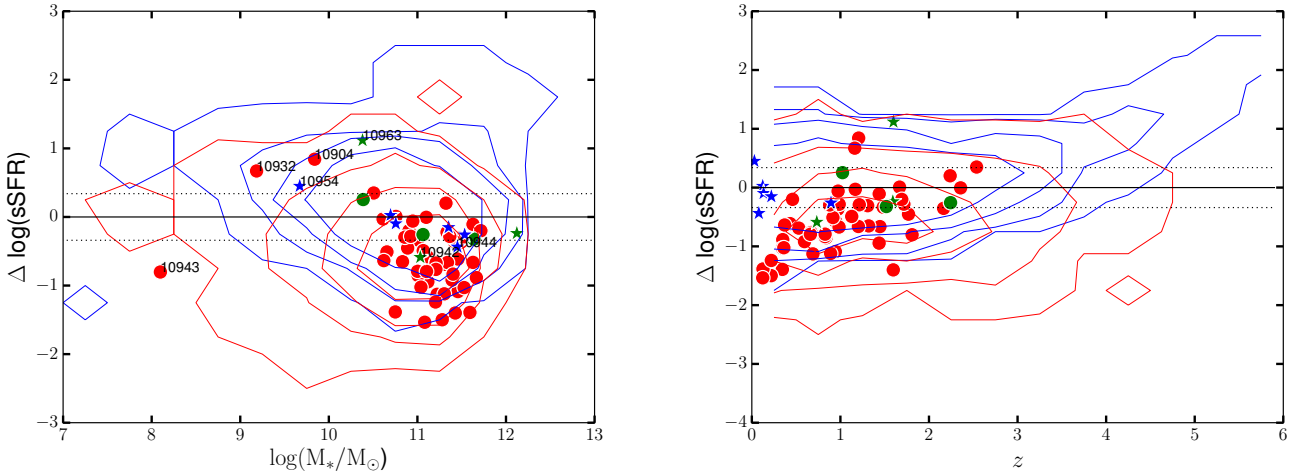

Fig. 5. ΔsSFR, the logarithmic difference between the specific SFR and the specific SFR of objects lying on the MS and at the same redshift, versus stellar mass M_* (see Delvecchio et al. 2017, for details on SFR calculation) shown on the left, and versus redshift z on the right. Symbols: red circles are the multi-component objects classified as AGN at 3 GHz VLA-COSMOS (objects that exhibit jets or lobes), as shown in Table A.1; blue stars are multi-component SFGs (see Sect. 2 for classification); green circles or stars are multi-component objects with uncertain classification (see Sect. 3.1), with circles used for AGN and stars for SFG based on the radio excess flag (see Sect. 3.1); the blue contours represent the single-component SFGs (objects that show no radio excess; Delvecchio et al. 2017) and the red contours are for single-component AGN (radio excess objects). The black solid and dashed lines show the main sequence for star-forming galaxies and its dispersion (Whitaker et al. 2012).

with the exception of 10963 which lies in the starburst (SB) region of the ΔsSFR–M_* diagram, and of 10942 that lies below the MS.

Furthermore, we investigate whether the six objects with uncertain classification have a VLBA counterpart in COSMOS (Herrera Ruiz et al. 2017). A cross-correlation does not give a match, implying that within the sensitivity of the VLBA observations (10 μJy at milli-arcsecond resolution of 16.2×7.3 mas^2) none of these six objects is associated with a bright point-like AGN. Finally, we use the radio excess flag[2] from Delvecchio et al. (2017) to further investigate whether these six objects with uncertain classification are AGN or SFGs. Based on this criterion, excess radio emission above what is expected from star formation should originate from AGN, thus radio excess can be used to separate AGN from SFGs. Based on that, 10942, 10963 and 10964 are SFGs, while 10939, 10940 and 10941 are AGN as the latter display excess radio emission, and we classify them as such for the rest of our analysis (see also Table A.1). We note that 10942 lies below the MS on the ΔsSFR–M_* diagram in the quiescent AGN region, but based on the radio excess parameter and the fit to the infrared SED (see Table 1), this is a clear SFG.

The few multi-component AGN in our sample at $z > 2$ are found within the MS, suggesting their hosts are star-forming galaxies. On the other hand, at $z < 2$ radio AGN occupy regions just below the scatter in the MS, with some exceptions within the MS and one above it. We also see that at low-z, multi-component AGN lie in their majority in the quiescent region and occupy massive hosts ($>10^{10.5}$ M_*).

Compared to the rest of the AGN at 3 GHz VLA-COSMOS shown by the density contours in Fig. 5, multi-component AGN lie at lower redshifts (up to $z \sim 2.5$) but occupy a similar parameter space. On the other hand, we do not find multi-component AGN above $z > 2$ in the quiescent region. At 3 GHz VLA-COSMOS depth we do not reach the sensitivity to identify diffuse multi-component sources that lie at high redshifts and in the quiescent region, as single-component AGN do. In fact, single-component AGN are located on the MS for SF and the green valley and/or quiescent region for up to redshifts of four, as seen in Fig. 5. Interestingly, the latter are also found above the MS at very high redshifts.

3.2. Types of multi-component objects at 3 GHz

Here we present the types of multi-component objects we encounter at 3 GHz VLA-COSMOS. These can be separated into two broad classes, AGN or SFGs. A detailed description of all the multi-component sources presented can be found in Appendix D.

3.2.1. The AGN multi-component radio sources at 3 GHz

Based on our classification, at 3 GHz VLA-COSMOS we find 58 radio AGN. Some display peculiar radio structure that shows interaction with the intergalactic environment. Following visual inspection, we identified different categories for the AGN multi-components in our sample. We note that, as classification depends on the surface brightness and frequency of the survey, as well as resolution, the same objects could be classified differently under different conditions.

We deem:

1. Head-tail (HT): One-sided radio AGN that show radio emission in the core and have one-sided jet attached to the core emission (2/58 AGN sources; Appendix D.1.1).
2. Core-lobe (CL): One-sided radio AGN that show radio emission in the core and have one-sided lobe not attached to the core emission (10/58 AGN sources; Appendix D.1.1).
3. Wide-angle-tail (WAT): FRI or FRII radio AGN with bent jets or lobes. The bending of the jets or lobes is the result of ram pressure while the source moves through the ICM (e.g. Sakelliou & Merrifield 2000). These show an inner-jet bend close to the core (9/58 AGN sources; Appendix D.1.2).
4. Z-/X-shaped (XZ): Objects that show signs of Z- or X-shape radio structure. This can be either due to a restarted AGN or axis reorientation (8/58 AGN sources; Appendix D.1.3).

[2] This radio excess flag is presented in Delvecchio et al. (2017), and can be used to separate AGN from SFGs. Excess radio emission above what is expected from star formation suggests the object is an AGN.

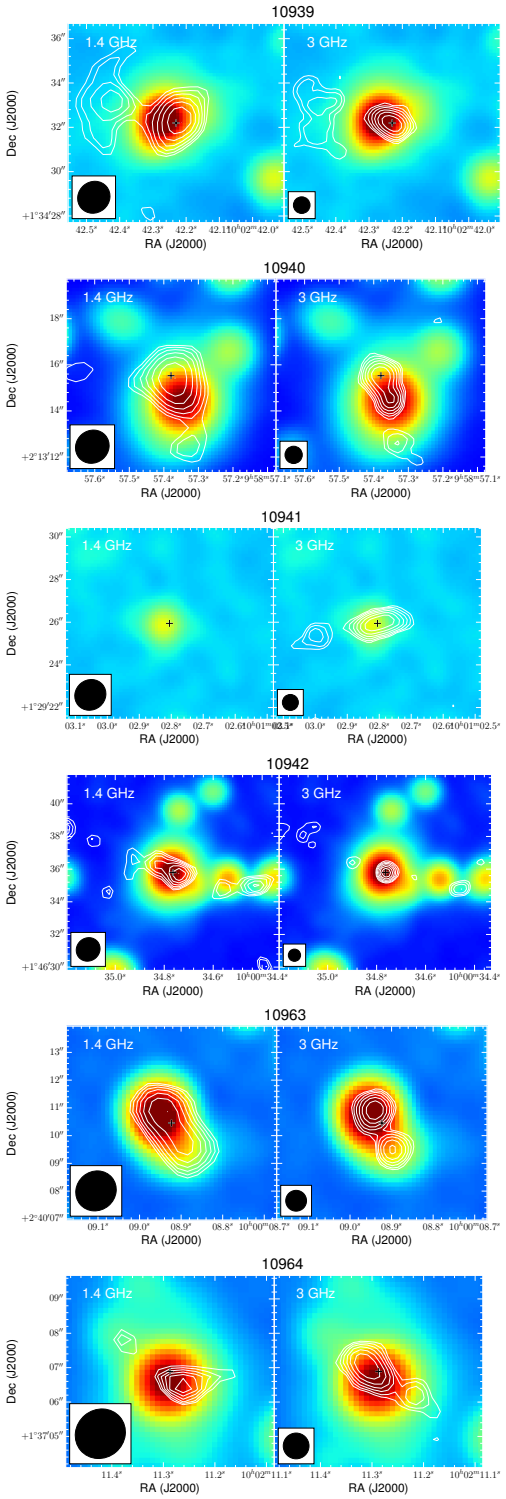

Fig. 6. The six multi-component objects at 3 GHz with uncertain classification (see Sect. 3.1). Images are described in Fig. 1.

5. Bent-tail (BT): Objects that show an outer-jet bend that is not a result of movement of the sources through the ICM, but due to the outer part of the jet interacting with a denser medium (3/58 AGN sources; Appendix D.1.4).
6. Symmetric AGN (SYM): Radio AGN in which their jets or lobes form 180° angle in respect to each other (26/58 AGN sources; Appendix D.1.5).

According to the above classification and the radio structure of the 3 GHz multi-component AGN, we find a large number of peculiar, that is, disturbed or bend sources (32 out of 58), while 20 of them show intense bending in their radio structure that deviates from a straight line (see Fig. D.7). We discuss this further below in Sect. 4.2. A detailed description of the classification can be found in Appendix D. These sub-classes are also presented in Table A.1, as part of the radio classification.

3.2.2. Multi-component SFGs

Our classification yields nine SFGs amongst the multi-component objects at 3 GHz VLA-COSMOS. These are presented in Fig. D.5 in Appendix D. The advantage of high-resolution observations is that we are able to resolve out star-forming regions within the galaxy disk (e.g. 10951 and 10965, see Fig. D.5 in Appendix D). The most striking object in this sub-sample is 10944. This is the only object in COSMOS that shows a well-resolved radio ring and a compact core radio emission. Nevertheless, it is not associated with an AGN, based on multi-wavelength data. We discuss this in detail in Appendix D.2.1 in Appendix D.

Furthermore, 10965 is quite an interesting object when it comes to disentangling radio AGN from SFGs. Classifying this object solely by looking at its radio map can be misleading. Depending on one's point of view, this can look either like an AGN where the jets are bent due to interaction with the environment, or like a disk of a star-forming galaxy.

4. Discussion

In this section, we discuss the effects of the high resolution (0.75 arcsec) and sensitivity (rms = 2.3 μJy beam^{-1}) of the VLA-COSMOS Large Project at 3 GHz in the context of multi-component sources.

4.1. Hosts of multi-component sources at 3 GHz VLA-COSMOS

In Sect. 3.1 we demonstrated that multi-component objects in our sample occupy a similar parameter space as single-component 3 GHz sources in the ΔsSFR versus M_* diagram (Fig. 5). They also have similar sSFRs to single-component AGN and SFGs, but lie at lower redshifts. A small fraction of the multi-component objects are SFGs (~13%) and are found within the MS. The rest are AGN (~87%) and are preferentially located below the main sequence.

Active galactic nuclei are believed to be responsible for quenching in situ star formation in star-forming galaxies lying in the MS through feedback (e.g. Hopkins et al. 2008; Combes 2015), due to their jet emission (radio-mode feedback) or in the form of winds (quasar-mode feedback; Combes et al. 2013, 2014). Hydrodynamical simulations show that AGN feedback transforms spiral galaxies into ellipticals (Dubois et al. 2013). So objects are expected to transition from the MS to the red-and-dead AGN region of the SFR–M_* plane passing through the green valley (e.g. Leslie et al. 2016). This scenario is supported by the high fraction of AGN within the green valley in studies such as 3D-HST/CANDELS ($0.5 < z < 2.5$, Gu et al. 2018). Nevertheless, studies in the COSMOS field from X-ray detected AGN showing far-IR emission (Mahoro et al. 2017; Lanzuisi et al. 2017), which lie in the green valley, show that AGN feedback plays a role in star formation, but not necessarily by quenching star formation. Silk et al. (2014) discuss how AGN outflows can enhance star formation through the compression of

dense clouds within the ISM. In our sample, all multi-component AGN display clear signs of jets or lobes by definition. The ones located in the green valley could suggest that AGN radio-mode feedback is in place, but it is not necessarily negative.

At very low-z ($\sim$0.5), in particular, we have multi-component AGN in the quiescent region, the majority all lying in massive hosts ($>10^{10.5}\,M_*$). Although this picture agrees with the scenario of passive evolution of galaxies, read-and-dead galaxies are indirect evidence for AGN feedback (see Fabian 2012).

Active galactic nuclei feedback is not necessarily the only mechanism responsible for quenching star formation. For example, Schawinski et al. (2014) propose a scenario for late-type spiral galaxies where once the cosmological inflow of gas has stopped, the galaxy leaves the MS while still converting gas and dust to stars, but at slower rates, until it becomes a red-and-dead late-type spiral, several Gyr later. We suspect that something similar is happening to the multi-component SFGs in our sample, 10942 and 10944, which lie below the MS. These objects are presented in detail in Appendix D.

In conclusion we see that multi-component AGN at 3 GHz in COSMOS occupy in their majority the green valley and quiescent region of Fig. 5, which suggests they can be responsible for star formation quenching. Also, the multi-component AGN seem to be representative of the general AGN population. Regarding the multi-component SFGs, they mainly occupy the MS for SF.

4.2. Investigating the high number of bent/disturbed sources at 3 GHz VLA-COSMOS

We have reported a large number (32 out of 58) of peculiar sources associated with AGN within the multi-component sample. These either show interaction with their IGM (e.g. 10950) or with the ICM (e.g. 10913, 10956). In Appendix D we describe the shapes of these objects in more detail. The important question that emerges is why do we have so many bent sources within 2.6 deg^2 of COSMOS, down to very small linear sizes.

In order to understand the reason behind this, we match the 3 GHz multi-component AGN sample (58 objects) to the X-ray group sample (247 groups at $0.08 \leq z < 1.53$) of Gozaliasl et al. (2019) from *Chandra*/*XMM-Newton* data in COSMOS (see also George et al. 2011). By X-ray groups we refer to a set of galaxies with a common dark matter halo (George et al. 2011). The X-ray groups have halo masses (M_{200}) of the order of $10^{12-14}\,M_\odot$ (see Gozaliasl et al. 2019). We use a search radius defined by the virial radius (R_{200}) of each group and the corresponding redshift of the source (see Table A.1), with $\Delta z = \pm 0.007 \times (1 + z_{\rm xgroup})$ to match the photometric redshift accuracy (Laigle et al. 2016).

We find 12 out of 58 ($\sim$21%) multi-component AGN (10902, 10910, 10912, 10913, 10918, 10933, 10948, 10950, 10953, 10956, 10958, 10966) within an X-ray group in COSMOS. From these objects, three are symmetric AGN (10902, 10948, 10953). We note that 10956 is a member of three X-ray groups, which is already known from the study of Smolčić et al. (2007), who report that we could be seeing the formation of a large cluster which is being assembled by several smaller groups. Thus, nine out of 58 ($\sim$16%) multi-component AGN that lie within X-ray groups in COSMOS exhibit peculiarities in their radio structure.

The rest of the AGN multi-component objects (46 out of 58; $\sim$79%) are not within the Gozaliasl et al. (2019) X-ray groups in COSMOS, thus we assume they lie in the field, or they are at redshifts not probed by the current X-ray data. Still, they might lie in mass halos below $<1.5(1+z)\times10^{13}\,M_\odot$ not probed by our current X-ray data (see Fig. 4 of Gozaliasl et al. 2019).

From the AGN outside X-ray groups, 23 out of 46 ($\sim$50%) show peculiarities in their radio structure. These belong to one of the sub-classes described in Sect. 3.2.1 (excluding symmetric AGN). We note that of the 23, four lie at redshifts above 1.53 (10915, 10929, 10941, 10943) and are not in the current X-ray group catalogue, and for one (10924) we have no redshift measurement. This leaves us with 18 multi-component AGN with peculiarities[3] that do not lie within the X-ray groups in COSMOS of Gozaliasl et al. (2019).

As we discuss in Appendix D.1.3, the Z/X shape can be a result of several scenarios, which involve galaxy merging and restarting of AGN activity (e.g. Gopal-Krishna et al. 2012). WATs are the result of ram pressure on the source moving through the ICM (e.g. Sakelliou & Merrifield 2000), as described in Appendix D.1.2 (e.g. 10956). Also, WATs are known to trace clusters of galaxies (e.g. Smolčić et al. 2007). Thus these objects can be used to identify groups of galaxies with smaller halo masses than probed by the current X-ray observations in COSMOS. Core-lobe sources that do not lie within the known X-ray groups in COSMOS might be old AGN that started to fade away, or they may lie within smaller groups not identified at X-rays (e.g. 10903, 10924). The rest of the objects outside X-ray groups are the one-sided head-tail sources and the bent-tail sources (10917 (BT), 10947 (HT), 10955 (HT)). We believe the reason for the interruption of the jet path in these three bent sources is a dense immediate environment outside the galaxy, the circum-galactic medium.

We note that within the X-ray groups of Gozaliasl et al. (2019) lies the multi-component SFG of our sample, 10965.

To summarise, from the 32 AGN with peculiarities and bends in their radio structure, we find ten inside X-ray groups and 18 outside of groups, while four are above the redshift range of the X-ray group catalogue, and one has no redshift. The fraction of AGN disturbed objects outside X-ray groups to the total number of AGN within groups (18/12) is significantly higher than the fraction of disturbed AGN within groups to the total AGN within groups (9/12). The large number of bent sources outside groups suggests two things:

1. We are probing density environments that cannot be probed by the current X-ray observations in COSMOS, that is less dense groups with halo masses below $<1.5(1+z)\times10^{13}\,M_\odot$. These objects can be used to identify small halo mass groups not currently identified by X-ray observations. An interesting question that arises is how the IGM affects the radio structure of AGN.
2. The COSMOS field is filled with a large number of bent radio sources associated with AGN. The latter can either be small or large in their size, or have diffuse radio structure. We have described a plethora of peculiarities in this group of objects. This is a result of the 0.75 arcsec resolution, which allows us to dive into the substructure of these sources and reveal objects that could not have been identified in surveys with poorer resolution. This is evident in Table 3 where we compare the ATLAS survey in the *Chandra* Deep Field-South (CDFS) field (Norris et al. 2006), which has an angular resolution of 10 arcsec and contains 41 multi-component sources. At 3 GHz we have a larger number of multi-component sources than in ATLAS CDFS, and we identify these as deep as 100 μJy, in contrast to ALTAS CDFS.

[3] In detail, there are five CL (10903, 10927, 10939, 10940, 10945), two HT (10955, 10957), five WAT (10900, 10931, 10949, 10952, 10962), four Z-/X-shaped (10909, 10914, 10919, 10935) and two BT (10917, 10947).

Table 3. Comparison of 1.4 GHz VLA-COSMOS and ATLAS multi-components per flux density bin.

Sample	Area	rms	Resolution	N_m/N_{tot}	N in $S_{1.4\,GHz}$ bins								
	(deg^2)	(μJy beam^{-1})	(arcsec)		0.01–0.1	0.1–0.6	0.6–1	1-6	6–10	10–60	60–100	100–160	>160
									(mJy)				
3 GHz VLA-COSMOS	2.6	2.3	0.75	67/10,830	0	11	6	25	4	17	3	1	0
ATLAS-CDFS	3.7	30	10	41/726	0	0	1	13	7	14	3	1	2

Notes. Comparison of 3 GHz VLA-COSMOS multicomponent sources to the multi-component sources in the ATLAS 3.7 deg^2 *Chandra* Deep Field-South (CDFS) field (Norris et al. 2006). ATLAS multi-components are identified from the flag CID in Table 6 of Norris et al. (2006). 3 GHz flux densities for COSMOS multi-component sources have been converted to 1.4 GHz fluxes using a typical steep spectrum index $\alpha = 0.8$. N_{tot} is the total number of radio sources in the survey and N_m the number of multi-component sources. The rest of the columns show the number of multi-component sources per flux density bin, from 10 μJy to 2000 mJy.

4.3. Multi-component AGN and SFG disentangling, and future surveys

Deep radio surveys such as the 3 GHz VLA-COSMOS, despite their advantage in detecting on the order of ten thousand objects in a very small patch of sky (2.6 deg^2), impose challenges when it comes to disentangling AGN and SFG populations of radio sources, which can have implications on how one can automatically identify sources in a radio survey. Here we briefly discuss the difficulties faced by current automatic algorithms in properly identifying such sources and disentangling the plethora of radio structures, given the upcoming radio surveys such as the square kilometre array (SKA) and precursors.

As we have demonstrated with the example of 10965 (see Fig. D.7), classifying AGN and SFGs solely by their radio images can lead to mis-classifications. Source 10965 resembles a bent-tail radio AGN at 3 GHz, when in fact what we observe is emission from the face-on disk of the SFG. An AGN diagnostic that is purely based on the radio structure can be misleading, especially for surveys that are dominated by SFGs at faint flux densities, like the 3 GHz VLA-COSMOS (see Fig. 13 of Smolčić et al. 2017b). This is the reason we use the UltraVISTA χ^2 map in combination with the radio maps to match the blobs in Sect. 2.1.

High angular resolution (milli-arcsec) radio observations such as very long baseline interferometry (VLBI) are often used to disentangle AGN and SF. This is a good diagnostic, but it also has its limitations. Although a source needs to have brightness temperature $\sim 10^6$ K to be observed with VLBI, there are cases of SF objects reaching those high values (Kaviraj et al. 2015; Herrera Ruiz et al. 2017). Indeed, many studies support that not even VLBI observations can disentangle AGN and SF in some cases, for example at higher redshifts (Herrera Ruiz et al. 2017), or in extreme objects such as Arp 220 (Lonsdale et al. 2006), and not every VLBI core can be associated to an AGN (Kaviraj et al. 2015).

The difficulty in disentangling AGN and SFGs has implications regarding automatic classification methods. As we have already discussed in Sect. 2.1, the current codes available for automatic identification of radio blobs or islands in radio mosaics do not perform a matching of the blobs, which is what is needed to identify multi-component objects. We performed a visual inspection to identify the objects that are composed of two or more blobs, combined them into a single parent source, and then updated the catalogue. Visually inspecting 10899 blobs is inefficient, subjective and time consuming. The method we describe in Sect. 2.1 is efficient and relatively fast, but has disadvantages when it comes to disentangling AGN from SFGs: if the objective is to select AGN, faint or diffuse sources with S/N and an extent below the cut will not be included in the selection.

As Hopkins et al. (2015) stress, there is no automated source finder for large surveys that can produce 100% completeness below the 10σ detection level; there is always a compromise when it comes to reliability and completeness of the catalogue produced by the available codes, which is the case with automatic algorithms. Attempting to fit extended sources with an automatic algorithm is a rather complicated task. If the algorithm uses Gaussian fits to find the extent of the source (e.g. PyBDSF), this can be proven difficult for large or diffuse sources. Thus, available codes provide much better results on compact sources after the exclusion of extended or diffuse objects. The development of source finders is necessary for upcoming radio surveys, i.e. algorithms that can handle both compact and extended sources, perform de-blending, blob association, eliminate spurious sources and artefacts, and can be reliable when it comes to completeness and detection levels. Current precursors for the Square Kilometre Array (SKA; Norris et al. 2013; Prandoni & Seymour 2015) are investing in the development of automatic techniques and testing their effectiveness on large data sets (e.g. the Canadian Initiative for Radio Astronomy Data Analysis – CIRADA[4]).

For an all-sky survey like the Very Large Array Sky Survey (VLASS[5]; Lacy et al. in prep.) for example, or the Evolutionary Map of the Universe survey (EMU[6]; Norris et al. 2011), which will be able to observe millions of radio sources down to 69 and 10 μJy beam^{-1} at angular resolutions of 2.5 and 10 arcsec, respectively, the challenge of matching radio blobs to their parent source will be a major issue. The expected number of sources for VLASS is 5×10^6 within 33 885 deg^2, and around 7×10^7 sources for EMU over the ~75% of the sky. Given that a survey like the 3 GHz VLA-COSMOS revealed ~11 000 sources in 2.6 deg^2 out of which 67 are multi-component, all-sky surveys should expect to find hundreds of thousands of multi-component sources.

Assuming VLASS reaches a resolution similar to 3 GHz VLA-COSMOS, the expected number of multi-component sources of VLASS would be $\sim 10^5$, given the depth and area coverage. However, for a factor of three worse resolution, the

[4] CIRADA is dedicated to the analysis of radio data from SKA and precursors.http://www.dunlap.utoronto.ca/instrumentation/cirada-canadian-initiative-for-radio-astronomy-data-analysis/

[5] https://science.nrao.edu/science/surveys/vlass

[6] http://www.atnf.csiro.au/people/Ray.Norris/emu/index.html. EMU is being observed by the Australian Square Kilometre Array Pathfinder (ASKAP) telescope.

expected number of multi-component sources is of the order of 10^4, making it not practical to visually inspect such a large number of sources. For EMU this number is smaller, of the order of 10^3, due to the much poorer resolution compared to 3 GHz VLA-COSMOS.

We believe that the COSMOS field is an excellent laboratory for testing new tools due to the plethora of multi-wavelength observations that can be used to cross-check whether an automatic algorithm performs well, that is, it provides enough information for a good identification of the source. Such codes can take into account the physical mechanisms responsible for the emission in a multi-frequency and multi-resolution parameter space, and not only rely on the appearance of the source at a specific frequency. The next step would be for developed algorithm to be used for future radio surveys, for which we do not have all the multi-wavelength information available. Along these lines, there are already efforts for the development of machine learning algorithms for classification by using self-organising maps (SOM) in LOFAR[7] for example (e.g. Shimwell et al. 2017, and Michiel Brentjens priv. comm.), as implemented in the PINK software by Polsterer et al. (2015). However, there are also methods that take into account the physical properties of objects and convolutional networks, as for example in Galaxy Zoo (Dennis Turp & Kevin Schawinski priv. comm.) and the EMU Collaboration (priv. comm.).

5. Conclusions

In this data paper we present the multi-component radio sources of the VLA-COSMOS Large Project at 3 GHz (Smolčić et al. 2017c), that is, those the radio sources composed of two or several radio blobs. These were identified by selecting the brightest and most extended objects in the catalogue, and were verified by visual inspection using a multi-wavelength approach.

The 3 GHz VLA-COSMOS survey demonstrates the importance of high resolution and sensitivity in identifying the substructure of radio sources within a field. Our study shows that we are probing populations that occupy lower density environments than what is probed by X-ray studies in COSMOS.

The multi-component objects can be either associated to AGN or to star-forming galaxies. Our results are summarised as follows:

1. We find 28 new multi-component sources that were not identified as such at 1.4 GHz by Schinnerer et al. (2007), due to the higher resolution of the 3 GHz observations.
2. We identify 58 AGN and nine star forming galaxies, based on the 1.4 and 3 GHz radio data and the UltraVISTA map for COSMOS.
3. From the 58 multi-component AGN we find two head-tail, ten core-lobe, nine WAT, eight double Z-/X-shaped, three bent-tail, and 26 symmetric AGN.
4. Due to the high resolution we are able to resolve the substructure of SFGs to smaller star-forming regions.
5. At the high-mass end ($>10^{10.5}\,M_\odot$), AGN lie in their majority below the MS for SF, in the green valley.
6. We find a large number (32 out of 58) of disturbed/bent radio AGN, 18 of which do not lie within X-ray groups in COSMOS ($0.08 \leq z < 1.53$ Gozaliasl et al. 2019).
7. The use of small, diffuse, bent radio AGN within COSMOS can pinpoint the location of small groups within COSMOS with halo masses $< 1.5(1+z) \times 10^{13}\,M_\odot$, not yet identified by COSMOS X-ray studies.
8. Disentangling AGN and SFGs using solely radio observations can be misleading, especially at the depths reached by 3 GHz VLA-COSMOS.

We believe that future radio surveys will benefit from the development of automatic algorithms that not only perform identification of radio blobs, but also match them in a single radio identification when these belong to the same parent source. These should include multi-wavelength information and the use of AGN diagnostics to disentangle AGN and SF, as they are both present at the low end of the radio luminosity function. COSMOS, with the plethora of auxiliary multi-wavelength data available, can be a laboratory for the development and testing of machine learning codes, which can be used for future radio surveys (SKA and precursors) in order to identify radio sources and eventually classify them based on type, without the need for extensive prior information.

Acknowledgements. We would like to thank the anonymous referee for suggestions that significantly improved the manuscript. We would also like to thank Mattia Vaccari for very useful comments. EV and SL acknowledge funding from the DFG grant BE 1837/13-1. Support for BM was provided by the DFG priority programme 1573 "The physics of the interstellar medium". EV, EFJA, AK, BM and FB acknowledge the support of the Collaborative Research Center 956, sub-project A1 and C4, funded by the Deutsche Forschungsgemeinschaft (DFG). KPM is a Jansky Fellow (NRAO, Caltech). VS, MN, KT, and JD acknowledge support from the European Union's Seventh Frame-work programme under grant agreement 337595 (ERC Starting Grant, "CoSMass").

References

Antonucci, R. 1993, ARA&A, 31, 473
Becker, R. H., White, R. L., & Helfand, D. J. 1994, ASP Conf. Ser., 61, 165
Berta, S., Lutz, D., Santini, P., et al. 2013, A&A, 551, A100
Bertin, E., Mellier, Y., Radovich, M., et al. 2002, in Astronomical Data Analysis Software and Systems XI, eds. D. A. Bohlender, D. Durand, T. H. Handley, (San Francisco: Astronomical Society of the Pacific), ASP Conf. Proc., 281, 228
Best, P. N., Ker, L. M., Simpson, C., Rigby, E. E., & Sabater, J. 2014, MNRAS, 445, 955
Burns, J. O. 1990, AJ, 99, 14
Cielo, S., Antonuccio-Delogu, V., Silk, J., & Romeo, A. D. 2017, MNRAS, 467, 4526
Civano, F., Elvis, M., Brusa, M., et al. 2012, ApJS, 201, 30
Civano, F., Marchesi, S., Comastri, A., et al. 2016, ApJ, 819, 62
Chabrier, G. 2003, ApJ, 586, L133
Combes, F. 2015, IAU Symp., 309, 182
Combes, F., García-Burillo, S., Casasola, V., et al. 2013, A&A, 558, A124
Combes, F., García-Burillo, S., Casasola, V., et al. 2014, A&A, 564, 1
Condon, J. J. 1992, ARA&A, 30, 575
Condon, J. J., Cotton, W. D., Greisen, E. W., et al. 1998, AJ, 115, 1693
da Cunha, E., Charlot, S., & Elbaz, D. 2008, MNRAS, 388, 1595
De Young, D. S. 2010, ApJ, 710, 743
Delvecchio, I., Smolčic, V., Zamorani, G., et al. 2017, A&A, 602, A3
Dubois, Y., Gavazzi, R., Peirani, S., & Silk, J. 2013, MNRAS, 433, 3297
Elvis, M., Civano, F., Vignali, C., et al. 2009, ApJS, 184, 158
Fabian, A. C. 2012, ARA&A, 50, 455
Fan, D., Budavari, T., Norris, R. P., & Hopkins, A. M. 2015, MNRAS, 451, 1299
Fanaroff, B. L., & Riley, J. M. 1974, MNRAS, 167, 31
George, M. R., Leauthaud, A., Bundy, K., et al. 2011, ApJ, 742, 125
Gopal-Krishna, Biermann, P. L., & Wiita, P. J. 2003, ApJ, 594, L103
Gopal-Krishna, Biermann, P. L., Gergely, L. A., & Wiita, P. J. 2012, Res. Astron. Astrophys., 12, 127
Gozaliasl, G., Finoguenov, A., Tanaka, M., et al. 2019, MNRAS, 483, 3545
Gu, Y., Fang, G., Yuan, Q., Cai, Z., & Wang, T. 2018, ApJ, 855, 10
Herrera Ruiz, N., Middelberg, E., Deller, A., et al. 2017, A&A, 607, 132
Hales, C. A., Murphy, T., Curran, J. R., et al. 2012, MNRAS, 425, 979
Hopkins, P. F., Hernquist, L., Cox, T. J., et al. 2008, ApJS, 175, 356
Hopkins, A. M., Whiting, M. T., Seymour, N., et al. 2015, PASA, 32, 37
Ishibashi, W., Auger, M. W., Zhang, D., & Fabian, A. C. 2014, MNRAS, 443, 1339
Kaviraj, S., Shabala, S. S., Deller, A. T., & Middelberg, E. 2015, MNRAS, 452, 774

[7] http://www.lofar.org

Koekemoer, A. M., Aussel, H., Calzetti, D., et al. 2007, ApJS, 172, 196
Laigle, C., McCracken, H. J., Ilbert, O., et al. 2016, ApJS, 224, 24
Lanzuisi, G., Delvecchio, I., Berta, S., et al. 2017, A&A, 602, 123
Leahy, J. P., & Williams, A. G. 1984, MNRAS, 210, 929
Leslie, S. K., Kewley, L. J., Sanders, D. B., & Lee, N. 2016, MNRAS, 455, 82
Lonsdale, C. J., Diamond, P. J., Thrall, H., Smith, H. E., & Lonsdale, C. J. 2006, ApJ, 647, 185
Mahoro, A., Pović, M., & Nkundabakura, P. 2017, MNRAS, 471, 3226
Marchesi, S., Lanzuisi, G., Civano, F., et al. 2016, ApJ, 830, 100
Mao, M. Y., Johnston-Hollitt, M., Stevens, J. B., & Wotherspoon, S. J. 2009, MNRAS, 392, 1070
Mao, M. Y., Sharp, R., Saikia, D. J., et al. 2010, MNRAS, 406, 2578
McMullin, J. P., Waters, B., Schiebel, D., Young, W., & Golap, K. 2007, in Astronomical Data Analysis Software and Systems XVI, eds. R. A. Shaw, F. Hill, & D. J. Bell (San Francisco, CA: ASP), ASP Conf. Ser., 376, 127
Miley, G. K., Perola, G. C., van der Kruit, P. C., & van der Laan, H. 1972, Nature, 237, 269
Mohan, N., & Rafferty, D. 2015, Astrophysics Source Code Library [record ascl:1502.007]
Moiseev, A. V., Smirnova, K. I., Smirnova, A. A., & Reshetnikov, V. P. 2011, MNRAS, 418, 244
Murphy, E. J. 2009, ApJ, 706, 482
Netzer, H. 2015, ARA&A, 53, 365
Norris, R. P., Afonso, J., Bacon, D., et al. 2013, PASA, 30, 20
Norris, R. P., Afonso, J., Appleton, P. N., et al. 2006, AJ, 132, 2409
Norris, R. P., Hopkins, A. M., Afonso, J., et al. 2011, PASA, 28, 215
Oklopčić, A., Smolčić, V., Giodini, S., et al. 2010, ApJ, 713, 484
Owen, F. N., & Rudnick, L. 1976, ApJ, 205, 1
Owen, Frazer N., & Laing, Robert A. 1989, MNRAS, 238, 357
Padovani, P. 2016, A&ARv, 24, 13
Prandoni, I., & Seymour, N. 2015, Proc. Advancing Astrophysics with the Square Kilometre Array (AASKA14), 67
Polsterer, K. L., Gieseke, F., & Igel, C. 2015, ASP Conf. Ser., 495, 81
Prestage, R. M., & Peacock, J. A. 1988, MNRAS, 230, 131
Rodriguez, C., Taylor, G. B., Zavala, R. T., et al. 2006, ApJ, 646, 49
Rudnick, L., & Owen, F. N. 1976, ApJ, 203, 107
Saikia, D. J., & Jamrozy, M. 2009, Bull. Astron. Soc. India, 37, 63
Sakelliou, I., & Merrifield, M. R. 2000, MNRAS, 311, 649
Sanders, D. B., Salvato, M., Aussel, H., et al. 2007, ApJS, 172, 86
Schinnerer, E., Smolcic, V., Carilli, C. L., et al. 2007, ApJS, 172, 46
Schinnerer, E., Sargent, M. T., Bondi, M., et al. 2010, ApJS, 188, 38
Schoenmakers, A. P., de Bruyn, A. G., Röttgering, H. J. A., van der Laan, H., & Kaiser, C. R. 2000, MNRAS, 315, 371
Seymour, N., Huynh, M., Dwelly, T., et al. 2009, MNRAS, 398, 1573
Silk, J., Di Cintio, A., & Dvorkin, I. 2014, Proc. Int. School Phys. Fermi, 186, 137
Simpson, C. 2017, R. Soc. Open Sci., 470522
Shimwell, T. W., Röttgering, H. J. A., Best, P. N., et al. 2017, A&A, 598, 104
Smolčić, V., Schinnerer, E., Finoguenov, A., et al. 2007, ApJS, 172, 313
Smolčić, V., Ciliegi, P., Jelić, V., et al. 2014, MNRAS, 443, 2590
Smolčić, V., Novak, M., Delvecchio, I., et al. 2017a, A&A, 602, 6
Smolčić, V., Delvecchio, I., Zamorani, G., et al. 2017b, A&A, 602A, 2
Smolčić, V., Novak, M., Bondi, M., et al. 2017c, A&A, 602, 1
Schawinski, K., Urry, C. M., Simmons, B. D., et al. 2014, MNRAS, 440, 889
Symeonidis, M., Kartaltepe, J., Salvato, M., et al. 2013, MNRAS, 433, 1015
Taniguchi, Y., Scoville, N., Murayama, T., et al. 2007, ApJS, 172, 9
Taniguchi, Y., Kajisawa, M., Kobayashi, M. A. R., et al. 2015, PASJ, 67, 104
Tisanić, K., Smolčić, V., Delhaize, J., et al. 2019, A&A, 621, A139
Williams, W. L., & Röttgering, H. J. A. 2015, MNRAS, 450, 1538
Willott, C. J., Rawlings, S., Blundell, K. M., & Lacy, M. 1999, MNRAS, 309, 1017
Whitaker, K. E., van Dokkum, P. G., Brammer, G., & Franx, M. 2012, ApJ, 754, 29
Zhao, J.-H., Burns, J. O., & Owen, F. N. 1989, AJ, 98, 64

Appendix A: Additional table

Table A.1. Multi-component radio properties.

3 GHz		RA	Dec	$S_{3\,\mathrm{GHz}}$	$S_{\mathrm{core}\ 3\,\mathrm{GHz}}$	$S_{\mathrm{VLBA}\ 1.4\,\mathrm{GHz}}$	z	1.4 GHz ID	VLBA	Radio
ID	COSMOSVLA3	(h:m:s)	(d:m:s)	(mJy)	(mJy)	(mJy)		COSMOSVLADP	ID	Class
(1)	(2)	(3)	(4)	(5)	(6)	(7)	(8)	(9)	(10)	(11)
10900	J095908.31+024309.6	09:59:08.319	+02:43:09.62	35.170	18.485	18.772	1.308^{s}	J095908.32+024309.6	C0686	AGN-WAT
10901	J095758.04+015825.1	09:57:58.041	+01:58:25.18	18.160	9.555	12.099	2.239^{s}	J095758.04+015825.2	C0090	AGN-SYM
10902	J095823.31+022628.4	09:58:23.310	+02:26:28.45	46.160	0.094	–	1.168^{s}	J095822.93+022619.8	–	AGN-SYM
10903	J100208.75+024103.2	10:02:08.753	+02:41:03.29	6.950	6.480	6.096	1.213^{s}	J100208.75+024103.3	C2867	AGN-CL
10904	J100243.26+015945.0	10:02:43.266	+01:59:45.00	28.420	0.011	–	1.206^{p}	J100242.57+015938.7	–	AGN-SYM
10905	J100229.89+023225.1	10:02:29.894	+02:32:25.15	3.170	2.086	2.016	0.432^{s}	J100229.89+023225.2	C3026	AGN-SYM
10906	J100212.06+023135.0	10:02:12.120	+02:31:35.016	8.651	–	0.048	0.948^{p}	J100212.06+023134.8	C2899	AGN-SYM
10907	J100309.43+022714.1	10:03:09.432	+02:27:14.12	2.814	2.382	0.308	1.210^{p}	J100309.43+022714.2	C3265	AGN-SYM
10908	J100339.24+015546.6	10:03:39.240	+01:55:46.67	26.230	–	–	0.921^{p}	–	–	AGN-SYM
10909	J100007.90+024315.3	10:00:07.903	+02:43:15.34	6.828	0.212	0.191	1.438^{p}	J100007.90+024315.4 &J100008.13+024308.0	C1374	AGN-XZ
10910	J100049.59+014923.7	10:00:49.590	+01:49:23.71	5.867	1.306	0.835	0.530^{s}	J100049.58+014923.7	C1893	AGN-WAT
10911	J100114.85+020208.6	10:01:14.858	+02:02:08.67	3.425	1.221	0.729	0.971^{s}	J100114.85+020208.8	C2214	AGN-SYM
10912	J095802.10+021540.8	09:58:02.101	+02:15:40.87	1.220	0.954	0.923	0.943^{s}	J095801.42+021542.3 &J095802.10+021540.9	C0109	AGN-CL
10913	J100028.28+024103.3	10:00:28.285	+02:41:03.37	32.090	1.057	0.833	0.349^{s}	J100025.91+024144.0 &J100028.29+024103.3	C1641	AGN-WAT
10914	J100230.19+020913.2	10:02:30.195	+02:09:13.25	3.327	0.611	0.431	1.437^{p}	J100230.11+020912.4	C3031	AGN-XZ
10915	J095959.17+014837.7	09:59:59.172	+01:48:37.78	3.692	–	–	2.357^{p}	J095959.16+014837.8	–	AGN-XZ
10916	J100140.12+015129.7	10:01:40.125	+01:51:29.76	5.438	0.050	–	0.4594^{s}	J100140.12+015129.9 &J100140.12+015129.9	–	AGN-SYM
10917	J100152.21+024535.3	10:01:52.216	+02:45:35.39	1.523	0.401	–	1.446^{p}	J100152.18+024536.0	–	AGN-BT
10918	J095824.02+024916.1	09:58:24.021	+02:49:16.16	25.220	0.575	0.364	0.3446^{s}	J095824.02+024916.0 &J095826.03+024921.9	C0255	AGN-XZ
10919	J100114.13+015444.1	10:01:14.131	+01:54:44.17	3.157	0.262	0.157	1.483^{p}	J100114.12+015444.3	C2203	AGN-XZ
10920	J095839.25+013557.7	09:58:39.253	+01:35:57.70	1.975	0.095	–	1.668^{p}	J095839.24+013557.8	–	AGN-SYM
10921	J095834.09+022703.3	09:58:34.097	+02:27:03.31	0.981	0.458	0.047	1.318^{p}	J095834.09+022703.4	C0337	AGN-SYM
10922	J100343.12+023700.3	10:03:43.128	+02:37:00.38	24.150	0.348	–	1.596^{p}	–	–	AGN-SYM
10923	J100303.67+014736.0	10:03:03.674	+01:47:36.00	13.170	0.239	0.156	1.203^{p}	J100303.66+014736.0	C3231	AGN-SYM
10924	J095925.79+030100.5	09:59:25.797	+03:01:00.57	9.353	1.762	–	–	–	–	AGN-CL
10925	J095741.10+015122.4	09:57:41.106	+01:51:22.44	18.540	0.606	0.443	0.984^{p}	J095741.10+015122.5	C0027	AGN-SYM
10926	J095949.84+015650.3	09:59:49.848	+01:56:50.35	0.744	–	0.075	1.768^{p}	J095949.80+015650.7	C1152	AGN-SYM

Notes. Columns 1 and 2 is the 3 GHz VLA-COSMOS ID of the multi-component and the IAU name, respectively. Columns 3 and 4 give the sexadecimal RA and Dec of the radio position (J2000.0). Column 5 gives the flux density at 3 GHz in mJy as measured from the map using CASA down to a 2σ level in surface brightness. Column 6 is the core flux density measured by a gaussian fit on the core position (also down to a 2σ level), in mJy. Column 7 is the matched VLBA flux density at 1.4 GHz which corresponds to the core. Column 8 gives the redshift from the COSMOS2015 catalogue (Laigle et al. 2016); the character "*s*" denotes spectroscopic while "*p*" denotes photometric redshift. Column 9 is the associated VLA source ID at 1.4 GHz from Schinnerer et al. (2010), while in Col. 10 is the VLBA ID at 1.4 GHz from Herrera Ruiz et al. (2017). Column 11 general radio classification: either AGN or SFG based on radio structure at 1.4 and 3 GHz: AGN if it exhibits jets or lobes; AGN-CL for core-lobe and AGN-HT for head-tail AGN (see Appendix D.1.1); AGN-WAT for wide-angle-tail AGN (see Appendix D.1.2); AGN-XZ for Z-/X-shaped AGN (see Appendix D.1.3); AGN-BT for bent-tail AGN (see Appendix D.1.4); AGN-SYM for an AGN with symmetric radio structure (see Appendix D.1.5); SFG if radio emission cannot be associated with jets or lobes but rather follows the disk structure of the galaxy; a * denotes that the classification is based on the radio excess (see Sect. 3.1).

Table A.1. continued.

3 GHz		RA	Dec	$S_{3\,\mathrm{GHz}}$	$S_{\mathrm{core}\,3\,\mathrm{GHz}}$	$S_{\mathrm{VLBA}\,1.4\,\mathrm{GHz}}$	z	1.4 GHz ID	VLBA	Radio
ID	COSMOSVLA3	(h:m:s)	(d:m:s)	(mJy)	(mJy)	(mJy)		COSMOSVLADP	ID	Class
(1)	(2)	(3)	(4)	(5)	(6)	(7)	(8)	(9)	(10)	(11)
10927	J100101.98+020511.4	10:01:01.985	+02:05:11.46	1.055	0.013	–	0.915^{p}	–	–	AGN-CL
10928	J095822.49+024722.2	09:58:22.497	+02:47:22.20	11.640	0.054	–	0.8784^{s}	J095822.30+024721.3	–	AGN-SYM
10929	J100211.45+015458.0	10:02:11.451	+01:54:58.08	0.298	0.150	0.121	1.716^{p}	J100211.44+015458.2 &J100211.44+015458.2	C2896	AGN-CL
10930	J100231.43+015138.1	10:02:31.435	+01:51:38.18	0.578	0.134	0.071	2.165^{s}	J100231.41+015138.3	C3043	AGN-SYM
10931	J095828.64+014407.6	09:58:28.649	+01:44:07.69	0.867	0.147	–	0.5947^{s}	J095828.65+014407.7	–	AGN-WAT
10932	J095945.81+025924.3	09:59:45.815	+02:59:24.35	0.816	0.446	–	1.161^{p}	–	–	AGN-SYM
10933	J100043.18+014607.8	10:00:43.186	+01:46:07.87	39.300	3.349	2.525	0.346^{s}	J100043.17+014607.9	C1810	AGN-XZ
10934	J100047.58+020958.6	10:00:47.585	+02:09:58.63	0.380	0.106	–	0.669^{s}	J100047.58+020958.8	–	AGN-SYM
10935	J095927.25+023729.2	09:59:27.251	+02:37:29.28	2.382	0.105	–	0.9544^{s}	J095927.25+023729.2	–	AGN-XZ
10936	J100028.24+013508.5	10:00:28.240	+01:35:08.59	10.050	0.146	–	0.839^{s}	J100028.31+013507.8	–	AGN-SYM
10937	J095947.83+021023.9	09:59:47.832	+02:10:23.98	0.230	–	–	1.127^{p}	J095947.83+021024.1	–	AGN-SYM
10938	J100138.64+030157.7	10:01:38.640	+03:01:57.72	0.849	–	–	0.913^{p}	–	–	AGN-SYM
10939	J100242.23+013432.1	10:02:42.232	+01:34:32.19	0.367	0.112	–	1.519^{s}	J100242.23+013432.3 &J100242.42+013432.9	–	AGN*-CL
10940	J095857.36+021315.5	09:58:57.360	+02:13:15.52	0.204	–	–	1.024^{s}	J095857.37+021315.2	–	AGN*-CL
10941	J100102.64+012925.9	10:01:2.6400	+01:29:25.95	0.549	–	–	2.243^{p}	–	–	AGN*-CL
10942	J100034.76+014635.7	10:00:34.760	+01:46:35.79	0.374	0.054	–	0.7335^{s}	J100034.77+014635.9	–	SFG*
10943	J100104.99+013154.5	10:01:04.993	+01:31:54.58	0.406	0.030	–	1.809^{p}	J100105.10+013153.8 &J100105.10+013153.8	–	AGN-CL
10944	J095905.52+023809.9	09:59:05.525	+02:38:09.91	0.948	0.040	–	0.079^{s}	J095905.55+023810.27	–	SFG
10945	J100124.19+023049.9	10:01:24.198	+02:30:49.98	0.205	0.036	–	0.6895^{s}	–	–	AGN-CL
10946	J100144.04+025712.6	10:01:44.040	+02:57:12.67	0.116	–	–	0.893^{p}	–	–	SFG
10947	J095918.98+014035.9	09:59:18.980	+01:40:35.95	0.120	0.023	–	2.537^{p}	J095919.03+014036.0	–	AGN-SYM
10948	J100021.78+015959.9	10:00:21.781	+01:59:59.97	1.943	1.100	0.552	0.219^{s}	J100021.78+020000.2	C1552	AGN-SYM
10949	J100124.06+024936.6	10:01:24.069	+02:49:36.68	2.718	1.193	0.965	0.826^{s}	J100124.09+024936.3	C2347	AGN-WAT
10950	J095949.01+025516.3	09:59:49.015	+02:55:16.39	1.439	1.044	–	0.1258^{s}	–	–	AGN-WAT
10951	J095917.74+020927.8	09:59:17.741	+02:09:27.83	0.890	0.598	0.257	1.692^{p}	J095917.70+020923.2 &J095917.73+020927.9	C0781	AGN-SYM
10952	J100238.68+022152.1	10:02:38.683	+02:21:52.19	1.687	0.548	0.205	0.827^{s}	J100238.67+022152.1	C3087	AGN-WAT
10953	J100018.50+023256.2	10:00:18.506	+02:32:56.29	1.254	0.251	0.152	0.890^{s}	J100018.50+023256.5	C1510	AGN-SYM
10954	J100008.10+024554.5	10:00:08.106	+02:45:54.54	0.508	0.297	–	0.029^{s}	J100008.10+024554.5	–	SFG
10955	J100307.47+023655.8	10:03:07.477	+02:36:55.89	1.058	0.111	–	0.370^{p}	J100307.48+023655.9	–	AGN-HT
10956	J100027.44+022123.2	10:00:27.440	+02:21:23.28	4.379	0.078	–	0.2202^{s}	J100027.31+022111.3	–	AGN-WAT
10957	J100015.55+020731.4	10:00:15.559	+02:07:31.40	0.514	0.069	–	0.6612^{s}	J100015.55+020731.5	–	AGN-HT
10958	J100136.46+022642.0	10:01:36.464	+02:26:42.04	0.889	0.045	–	0.123^{s}	J100136.46+022641.8	–	AGN-XZ
10959	J100245.40+024516.1	10:02:45.405	+02:45:16.13	8.576	0.049	–	0.986^{p}	J100245.39+024519.8	–	AGN-SYM
10960	J100120.64+021816.6	10:01:20.640	+02:18:16.60	0.188	–	–	0.123^{s}	J100120.60+021817.9	–	SFG
10961	J095934.59+014924.4	09:59:34.592	+01:49:24.47	0.107	0.001	–	0.133^{s}	J095934.57+014923.6	–	SFG
10962	J102833.60+024248.0	10:28:33.600	+02:42:48.07	80.250	–	–	0.974^{p}	J100251.11+024248.5	–	AGN-WAT
10963	J100008.94+024010.9	10:00:08.941	+02:40:10.90	0.152	0.090	–	1.599^{s}	J100008.91+024010.3	–	SFG*
10964	J102154.00+013706.8	10:21:54.000	+01:37:6.882	0.092	–	–	1.592^{s}	J100211.24+013706.8	–	SFG*
10965	J100045.28+013847.4	10:00:45.286	+01:38:47.43	0.263	0.016	–	0.2204^{s}	J100045.32+013846.5	–	SFG
10966	J100106.73+013320.4	10:01:06.735	+01:33:20.43	0.861	0.032	–	0.361^{p}	J100106.76+013320.0	–	AGN-BT

Appendix B: Testing the effect of coarser resolution on the 3 GHz sources

To test how the coarser resolution can change the appearance of the 3 GHz multi-component sources, we degraded the resolution of the 3 GHz mosaic to match that at 1.4 GHz, and re-examined the objects. We find that ∼55% (37 out of 67) of the 3 GHz multi-component objects become single-component in the coarser resolution map, that is, the radio emission does not break between the components and the sources appear to be composed of a single radio blob in the 1.5 arcsec resolution 3 GHz mosaic[8]. Images are shown in Fig. D.7 in the Appendix, next to the actual 3 GHz resolution images for comparison.

Finally, in order to check whether we fully recover the flux from the source we cross-match the 3 GHz radio positions to the NRAO VLA sky survey (NVSS) (angular resolution 45 arcsec Condon et al. 1998) and the faint images of the radio sky at twenty-cm (FIRST) (angular resolution 5 arcsec Becker et al. 1994) radio-source surveys. We find 29 matches with NVSS within a 15-arcsec search-radius and 20 in FIRST. As a search radius for FIRST, we use 20 arcsec, except for the following sources due to their larger extent: 10901 (40″), 10910 (40″), 10913 (90″), 10925 (35″), 10928 (30″), and 10936 (40″). The resulting flux densities are given in Table C.1. We find that NVSS and FIRST flux densities are on average ∼ 29% and 43%, respectively, smaller than the 1.4 GHz COSMOS flux densities. To compare the FIRST and 3 GHz flux densities we use a typical steep radio spectral index of 0.8. We find that FIRST fluxes are on average ∼19% larger than fluxes at 3 GHz. We do not compare the NVSS to 3 GHz VLA-COSMOS flux densities due to the large difference in angular resolution. These differences can be a consequence of a simplistic assumption of the spectral index but also an effect of different resolution. We also note that, in cases, FIRST flux densities are much lower than the NVSS, or the 1.4 and 3 GHz. For example in 10935, only the north lobe is identified by FIRST, while the south lobe, which is diffuse, is not observed. Also, in 10910 the north lobe is not identified by FIRST resulting in the low flux density value in Table C.1. We note that sources without 1.4 GHz flux entry in Table C.1 lie outside the coverage of the survey.

Appendix C: Matching 3 GHz multi-component radio sources with their multi-frequency analogues

In this section we describe how we matched the multi-frequency radio catalogues for COSMOS to the 3 GHz multi-component sources presented in this paper. We use the data for COSMOS available from three catalogues, 324 MHz (Smolčić et al. 2014), 325 MHz (Tisanić et al. 2019) and 1.4 GHz (Schinnerer et al. 2007, 2010). In order to match the 3 GHz multi-component COSMOS objects we had to take into account: (i) the different angular resolution of each map from which the data were extracted from, and (ii) near-by sources that could blend with the parent source in cases of poorer resolution. This method was developed to be able to rely solely on catalogue information, rather than carrying out a full visual inspection of the radio maps. Due to the high resolution of the 3 GHz data of 0.″75, we are able to distinguish the sub-structure of these multi-component

[8] Multi-component objects at 3 GHz that become single-component sources after convolving the mosaic to 1.5 arcsec resolution: 10906, 10907, 10908, 10909, 10915, 10917, 10922, 10924, 10928, 10930, 10932, 10934, 10935, 10937, 10938, 10939, 10940, 10941, 10943, 10944, 10945, 10946, 10947, 10948, 10949, 10950, 10952, 10953, 10954, 10955, 10957, 10960, 10961, 10962, 10965, 10966.

Table C.1. FIRST and NVSS matches to 1.4- and 3 GHz VLA-COSMOS.

3 GHz	S (mJy)			
ID	1.4 GHz NVSS	1.4 GHz FIRST	1.4 GHz COSMOS	3 GHz COSMOS
(1)	(2)	(3)	(4)	(5)
10900	59.4	55.91^{3m}	60.51	35.17
10901	52.2	43.91^{3m}	53.03	18.16
10902	–	–	116.5	46.16
10903	11.6	10.01	10.61	6.950
10904	58.7	53.52^{2m}	64.60	28.42
10905	8.2	2.66	5.673	3.170
10906	17.4	16.28^{2m}	19.21	8.651
10907	5.2	4.43	5.271	2.814
10908	50.3	49.97^{2m}	–	26.23
10909	12.0	9.98^{2m}	12.99	6.828
10910	12.4	5.48^{2m}	15.10	5.867
10911	6.2	4.77^{2m}	7.509	3.425
10912	–	–	2.200	1.220
10913	73.1^{2m}	52.51^{3m}	82.83	32.09
10914	6.3	6.40^{2m}	7.751	3.327
10915	8.4	7.69	9.799	3.692
10916	11.1	7.84	12.92	5.438
10917	2.6	2.25	2.658	1.523
10918	50.9	34.43^{2m}	57.26	25.22
10919	6.2	4.99^{2m}	8.119	3.157
10920	4.9	2.55	4.706	1.975
10921	–	–	2.422	0.981
10922	58.0	52.04^{2m}	–	24.15
10923	–	–	37.02	13.17
10924	27.7	16.49^{2m}	–	9.353
10925	43.2	31.17^{3m}	47.23	18.54
10926	–	1.77	2.027	0.744
10927	–	–	3.428	1.055
10928	22.7	17.36^{2m}	30.12	11.64
10929	–	–	0.675	0.298
10930	–	–	1.173	0.578
10931	–	–	2.275	0.867
10932	–	–	–	0.816
10933	82.3	77.24^{2m}	88.17	39.30
10934	–	–	0.942	0.380
10935	5.9	1.94	6.548	2.382
10936	26.6	14.65^{2m}	29.13	10.05
10937	–	–	0.432	0.230
10938	–	–	–	0.849
10939	–	–	0.920	0.367
10940	–	–	0.411	0.204
10941	–	–	–	0.549
10942	–	–	0.107	0.374
10943	–	–	0.994	0.406
10944	–	–	2.815	0.948
10945	–	–	–	0.205
10946	–	–	–	0.116
10947	–	–	0.313	0.120
10948	–	–	2.625	1.943

Notes. Matches with FIRST (Becker et al. 1994) and NVSS (Condon et al. 1998) radio surveys within a 20″ and 15″ arcsec radius, respectively. Note that for the following sources we used a larger radius due to their entent: 10901 (40″), 10910 (40″), 10913 (90″), 10925 (35″), 10928 (30″), 10936 (40″). Also for 10913 we used a 90″ search radius in NVSS to recover the lobes. The surveys' archives (FIRST: `http://sundog.stsci.edu/cgi-bin/searchfirst` and NVSS: `http://www.cv.nrao.edu/nvss/NVSSlist.shtml`) were utilised for the search. The character m denotes multi-component source, and that the fluxes of the components have been added together, while a number if front of it indicates the number of blobs matched.

Table C.1. continued.

3 GHz	S (mJy)			
ID	1.4 GHz NVSS	1.4 GHz FIRST	1.4 GHz COSMOS	3 GHz COSMOS
(1)	(2)	(3)	(4)	(5)
10949	3.9	3.39	5.422	2.718
10950	–	1.87	–	1.439
10951	4.2	–	1.827	0.890
10952	4.0	–	4.533	1.687
10953	–	–	3.192	1.254
10954	–	–	1.387	0.508
10955	–	–	6.229	1.058
10956	–	–	17.04	4.379
10957	–	–	1.774	0.514
10958	–	–	2.305	0.889
10959	28.2	20.00^{2m}	35.14	8.576
10960	–	–	0.595	0.188
10961	–	–	0.334	0.107
10962	–	–	175.5	80.25
10963	–	–	0.302	0.152
10964	–	–	0.102	0.092
10965	–	–	0.526	0.263
10966	–	1.57	2.873	0.861

sources and disentangle them from near-by objects. However, in the case of the 325 MHz map, with angular resolution of 10 arcsec, we need to be careful when performing the matching not to include blended sources or mis-matches. For that reason the following automatic technique was applied.

The code is written in IDL and takes as priors the radio positions of the 3 GHz multi-component sources as reported in Table A.1. The purpose is to search within the area occupied by the multi-component source. For this we need the size of the source and the area it occupies. The linear projected sizes of these objects were measured by a semi-automatic machine learning technique that i) identifies extended blobs by using the skeleton of the source, ii) joins blobs that belong to the same parent source via a clustering algorithm, and iii) measures the linear projected size of the source in arcsec. The method is described in Vardoulaki et al. (in prep.; credit E. Jimenez-Andrade).

Now we can search within the area the source occupies. The actual search radius was set to size/1.5 to account for asymmetries in the lobe-core distance of some objects. However, just using a search radius does not remove near-by objects not associated with the parent source. For that reason a mask was applied to the 3 GHz stamps, and then the algorithm searches within the radius given by the linear size of the source.

The 3 GHz stamps were convolved to the coarser resolution of 10 arcsec[9], and all pixels below 3σ of the local rms were flagged. This mask was then used to approve and/or reject sources within the search radius. Therefore the algorithm gives a match when it satisfies two conditions: (i) radio position within the mask, and (ii) radio position within the search radius (size/1.5).

In some cases at 325 MHz, the 3 GHz multi-component sources were matched with more than one 325-MHz blob. These 325 MHz multi-component sources were joined automatically by the code and their flux densities were added together. An example is shown in Fig. C.1. The results of the matching are shown in Table 2. Multi-component sources that were joined together are marked with *m*.

[9] There is no need to re-grid as we are interested in creating a mask and using it in combination with the size of the source.

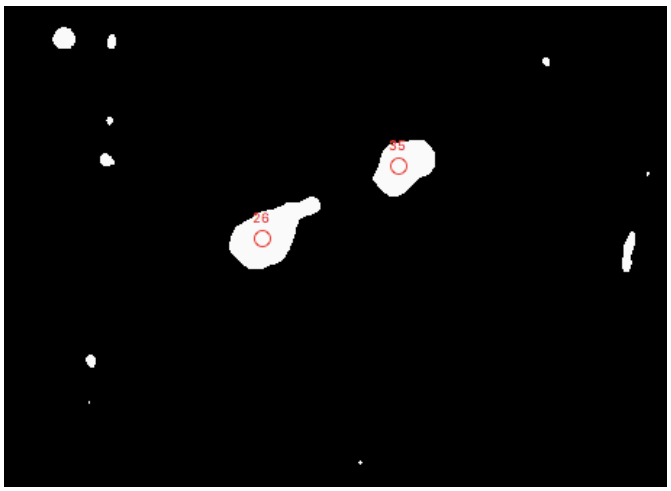

Fig. C.1. Example of 3 GHz stamp convolved to 10″ with 325-MHz radio positions within the stamp. The mask is shown in black and white, where flux densities above 3σ at 3 GHz are shown as white. Red circles mark the 325-MHz blob radio positions. Only circles inside the white area occupied by the 3 GHz source were matched to the 3 GHz multi-component source.

Appendix D: Notes on the objects

Here we present a detailed description of the multi-component sources at 3 GHz VLA-COSMOS. These are separated into two major classes, AGN or SFGs. We further separate AGN into classes based on their radio structure.

D.1. The AGN multi-component radio sources at 3 GHz

Based on our classification, at 3 GHz VLA-COSMOS we find 58 multi-component radio AGN. Some display a peculiar radio structure that shows interaction with their environment. Following visual inspection, we further identified different categories for the multi-component sources: head-tail (two) and core-lobe (ten) sources (Appendix D.1.1); wide-angle-tail sources (nine sources; Appendix D.1.2); Z-/X-shaped radio galaxies (eight sources; Appendix D.1.3); bent-tail (three sources; Appendix D.1.4), and 26 symmetric AGN, where the lobes form an angle of approximately 180° in respect to each other (Appendix D.1.5). These sub-classes are also presented in Table A.1, as part of the radio classification.

D.1.1. Head-tail and core-lobe multi-component radio sources at 3 GHz

This sub-class includes multi-component AGN radio sources that display one-sided emission. Either core emission and a single lobe (10903, 10912, 10924, 10927, 10929, 10939, 10940, 10941, 10943, 10945), or a one-sided radio jet called head-tail (10955, 10957). The core-lobe and head-tail objects in our sample are presented in Fig. D.1.

In more detail, 10903 shows a lobe to the east and core emission that slightly extends to the south-west.

Source 10902 displays core emission that is unresolved at 3 GHz and a lobe at the west of the source.

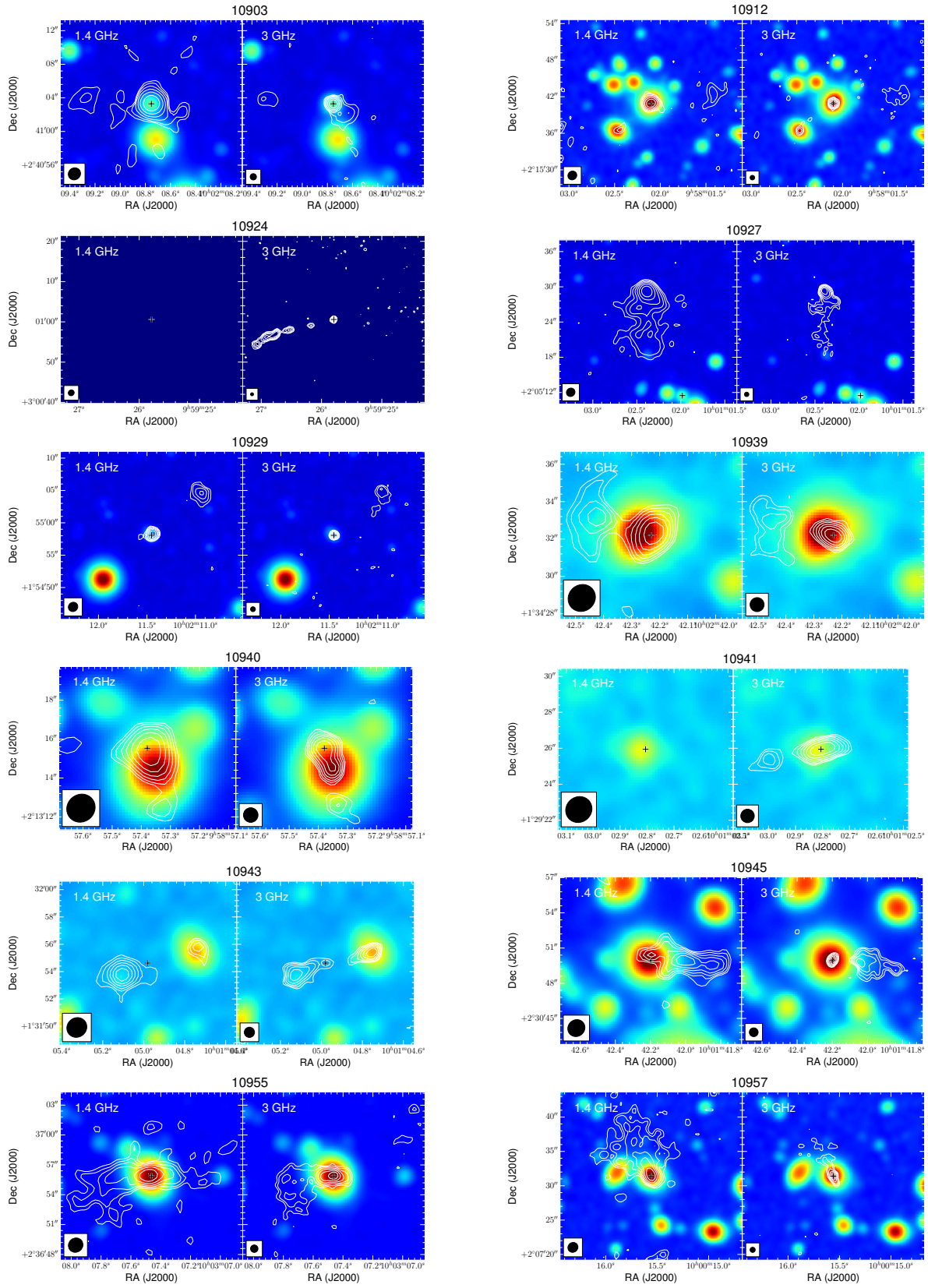

Fig. D.1. The ten core-lobe (10903, 10912, 10924, 10927, 10929, 10939, 10940, 10941, 10943, 10945) and two head-tail (10955, 10957) multi-component 3 GHz radio sources in COSMOS. Images described in Fig. D.7.

Source 10924 lies in a rather noisy region close to the edge of the 3 GHz map. It shows core emission and a jet to the east. We classify it as a possible core-lobe source.

Source 10927 displays a core and a single lobe, with the host identified to be on the south of the lobe ~7 arcsec away (see also counterpart catalogue, Smolčić et al. (2017b)). We note

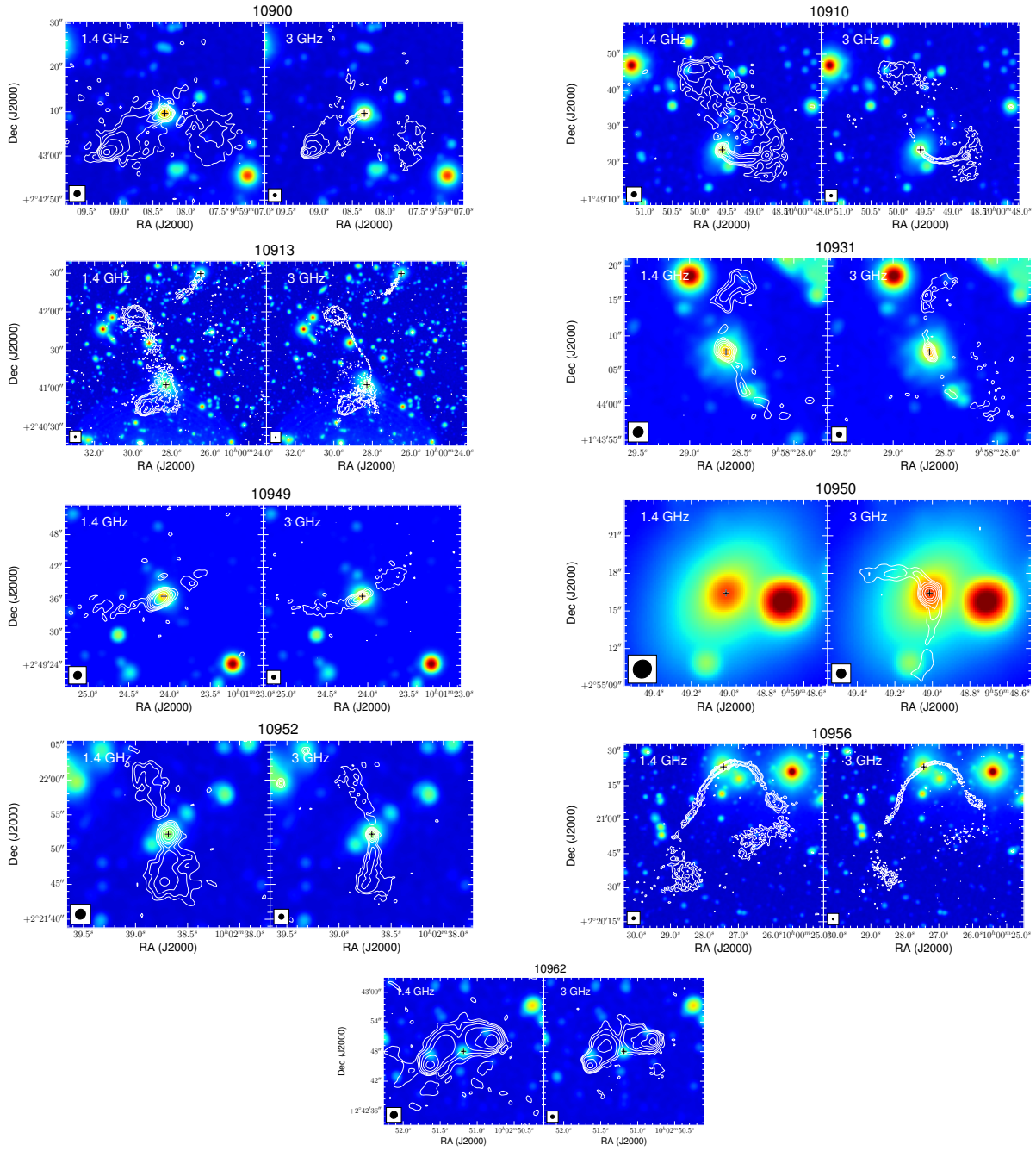

Fig. D.2. The nine wide-angle-tail multi-component objects at 3 GHz. Images described in Fig. D.7.

that this object could instead be a narrow-angle-tail radio source (Miley et al. 1972), that is, a WAT seen edge-on, and lies within an X-ray group in COSMOS from the catalogue of Gozaliasl et al. (2019). We classify it as a possible a core-lobe source.

Source 10929 is also a core-lobe source.

Source 10939 was initially in the uncertain class, but since it displays radio excess (see Sect. 3.1) we classify it as AGN; it also has a core-single lobe radio structure.

Source 10940 was classified as AGN based on its radio excess. It shows extended core emission, probably a blend of core and jet emission, and a lobe to the south.

Source 10941 was also classified as AGN based on its radio excess and is similar to 10940, with the lobe emission to the east. Source 10943 also shows slightly extended core emission and a radio lobe to the east.

Source 10945 shows a core-lobe radio structure at 3 GHz, while at 1.4 GHz is a head-tail. The enhanced resolution and sensitivity of the 3 GHz have resulted in this object being a multi-component at 3 GHz and classified as a core-lobe.

Source 10955 is one-sided at 3 GHz (head-tail), showing bending towards the edge of the lobe/jet-like radio structure.

Source 10957 is a diffuse head-tail radio source.

D.1.2. Wide-angle-tail sources at 3 GHz

Here we present the multi-component wide-angle-tail radio sources at 3 GHz VLA-COSMOS. In our sample, the most striking case of a WAT is 10956, known with the name CWAT-01 (Smolčić et al. 2007). It is a huge (~200 kpc long), bent, C-shaped radio structure, that has been previously studied by

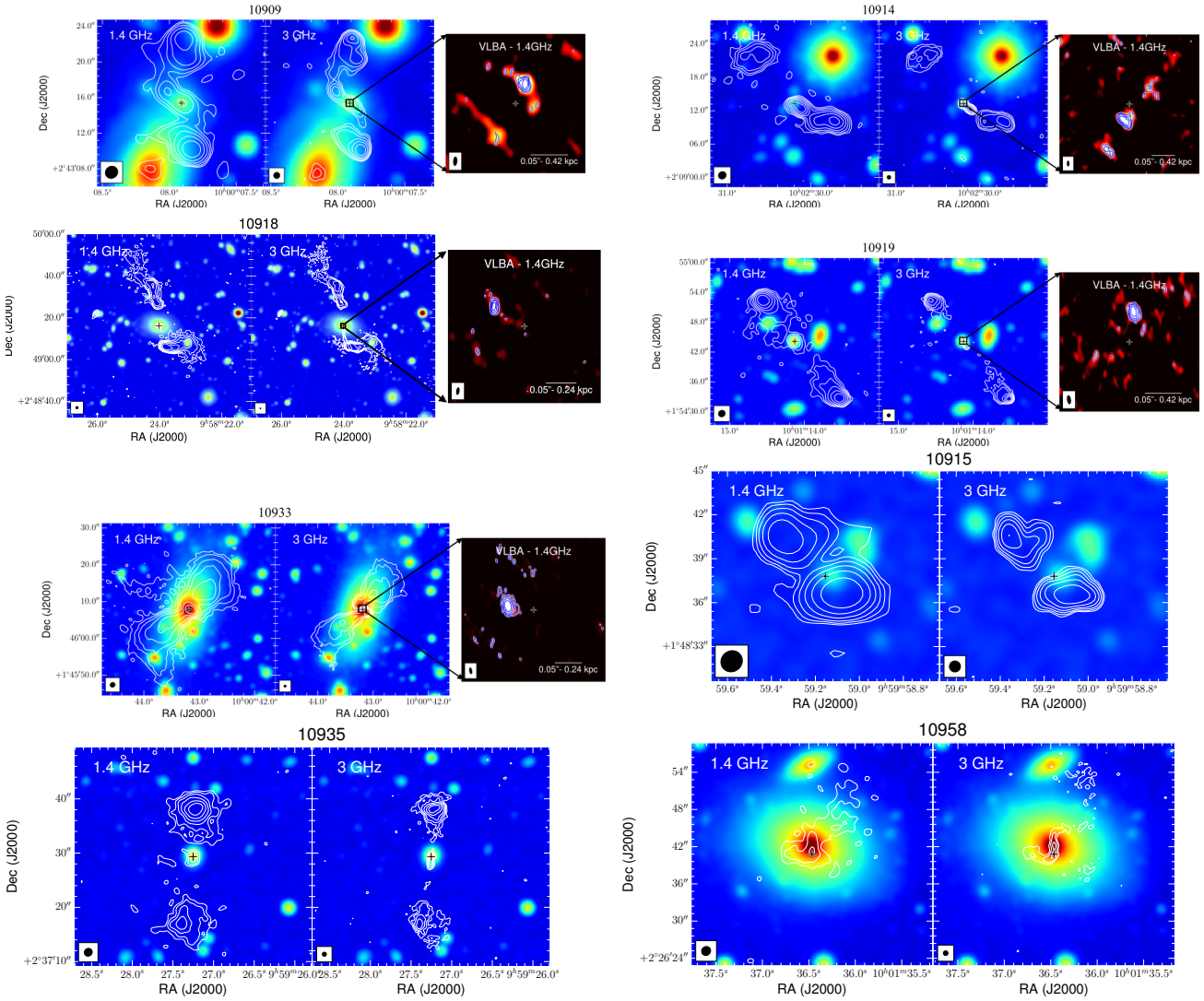

Fig. D.3. The eight double-double, Z-/X-shaped multi-component objects at 3 GHz. *Top panels*: five sources described in Appendix D.1.3 with double-double, Z-/X-shaped radio structure and VLBA observations. Each set of images gives the 1.4 GHz VLA (*left*), the 3 GHz VLA (*middle*) and the 1.4 GHz VLBA (*right*). *Left and middle panels*: similar to the ones in Fig. 1, while the *right panels* show the VLBA stamp corresponding to the nucleus; the corresponding radio contours start at 3σ increasing logarithmically, and the beam is 16.2×7.3 mas^2. The VLBA stamps of these objects do not show signs for double core system that could verify the existence of a binary SMBH in the centre of these objects, and which would give rise to a double-double radio structure. The three sources at the bottom lack VLBA identification. The radio/infrared overlays for all objects are described in Fig. D.7.

Smolčić et al. (2007) in great detail. They performed a Voronoi tesselation analysis and found that 10956 lies in a supercluster, where smaller clusters are actively forming a larger one with a total mass 20% of the Coma cluster. Other WAT multi-component radio sources at 3 GHz VLA-COSMOS are: 10900, 10910, 10913, 10931, 10949 (?), 10950, 10952 and 10962.

Source 10949 has a very small bend and is rather diffuse, so we caution the reader about the WAT.

Source 10962 is not a typical WAT. Although it is symmetric and the jets and lobes form an angle with respect to each other, the lobes seem to go backwards. This could probably be a projection effect, although we cannot rule out the case where the jet encounters a denser medium causing it to flow backwards towards the point of ejection (e.g. Cielo et al. 2017).

Source 10900 has a diffuse south lobe.

Source 10910 shows a bent jet on the south, leading to a diffuse lobe. This source was studied a few years ago by Oklopčić et al. (2010), who refer to it as CWAT-02.

In 10913 the jets seem dragged in the ICM forming an angle in respect to the original jet-emission path. The lobes themselves seem bent and slightly diffuse, suggesting the radio source is fading. 10931 is a very diffuse WAT.

Source 10950 is a small size WAT. Source 10952 has a diffuse north lobe.

The C-shaped radio structure in WATs is caused by strong interaction of the jets of the source with the environment (e.g. Owen & Rudnick 1976; Owen & Laing 1989; Zhao et al. 1989; Burns 1990; Smolčić et al. 2007; Mao et al. 2010). Ram pressure distorts the radio structure and forces the jets to bend backwards as the source moves through the ICM. For that reason, they are often used as probes or tracers of clusters of galaxies (e.g. Prestage & Peacock 1988; Owen & Laing 1989; Burns 1990; Smolčić et al. 2007). These types of objects show a bend on the inner part of the jets (inner-jet bend-radio sources), in contrast to objects showing bents on the part of the jet further away from the core (outer-get-bend radio sources). The bend in

the jet in the latter case is due to the jet interacting with a denser environment and not due to ram pressure from the movement of the source in its ICM. An example is object 10966 (not a WAT), where the outer parts of the jets are bent to almost 90° with respect to the jet ejection direction. This is actually classified as BT (see Appendix D.1.4).

Wide-angle-tail radio sources are often found inside clusters of galaxies and can be the result of the galaxy's movement inside a hot and dense intracluster medium (Rudnick & Owen 1976; Mao et al. 2009). The dense medium is what causes jets of the source to bend backwards due to ram pressure (Mao et al. 2009). This mechanism explains the bent shapes of WAT sources within our sample.

D.1.3. Double-double, Z-/X-shaped, and restarted AGN at 3 GHz

In the multi-component sample, we identify seven double-double or Z-/X-shaped AGN. These display double-double radio structure: 10909, 10914, 10915 (?), 10918, 10919, 10933, 10935 and 10958, as shown in Fig. D.3. Within the sources in our multi-component sample the following objects fall into the restarted AGN category due to their radio structure at 3 GHz: 10909, 10915, 10933, and 10935.

Source 10909 is a double-lobed radio AGN with the furthest away lobes being the oldest, while closer to the core it exhibits another double-lobed structure. This twisted radio structure is most probably not the result of movement of the source in the ICM as in that case we would see a WAT or head-tail source, depending on orientation. This strong resemblance to an X-shaped source might be due to a restarted AGN phase due to jet interruption or axis re-orientation, rather than a projection effect.

In 10915 we see only two unevenly shaped lobes and no core emission at 3 GHz.

Source 10918 displays a bend in the south lobe probably caused by interaction with a denser medium. The 3 GHz map shows in great detail the south jet leading to the bent lobe structure, which is not seen at 1.4 GHz. The bend in the north lobe is towards the opposite direction, thus it is placed in this Z-shaped class.

Source 10933 displays a rotation of the jet/lobe structure close to the centre of emission (marked by the black cross in Fig. D.3). This does not look like a projection effect as the two jet/lobe structures look alike and symmetric. Thus the radio structure is most probably a result of axis reorientation.

Source 10935 is a symmetric source that displays a double-double radio structure, which is based on the observation that at both 1.4 and 3 GHz the lobes are very diffuse, but there is a clear jet at 3 GHz, which could indicate restarted activity. Source 10958 is a rather peculiar object, which is S-shaped. The jets bent to opposite directions and seem to do that within the galaxy itself.

Radio sources that are Z-/X-shaped, that is, radio sources that have a double-double, Z-, or X-like radio structure, have been reported in past radio studies and are likely linked to recurrent AGN activity (see Gopal-Krishna et al. 2012, for a review). Episodic mass accretion onto a supermassive black hole results in two pairs (e.g. Schoenmakers et al. 2000) or even three pairs of radio lobes (e.g. Saikia & Jamrozy 2009). These can be well aligned (e.g. Schoenmakers et al. 2000), or can be X-shaped (e.g. Leahy & Williams 1984) or Z-shaped (e.g. Gopal-Krishna et al. 2003). The mechanisms behind this recurrent AGN activity can be either axis reorientation, also

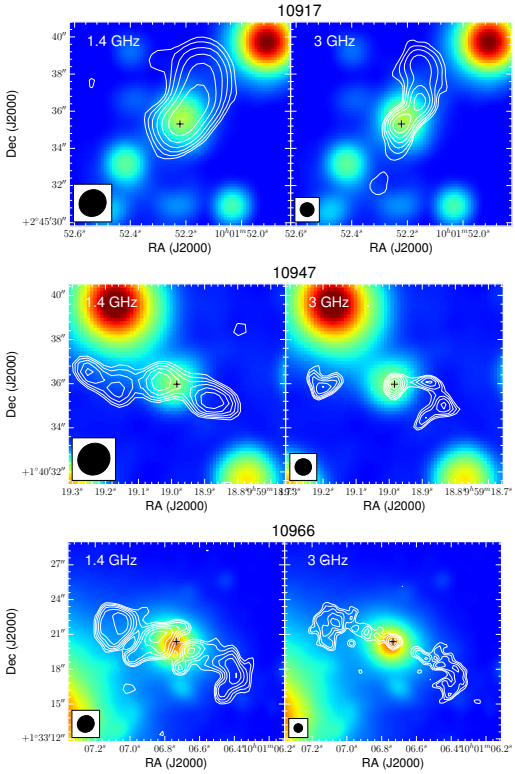

Fig. D.4. The three bent-tail 3 GHz radio sources in COSMOS, show interaction with a dense environment. Images are described in Fig. D.7.

known as "spin-flip" (e.g. Gopal-Krishna et al. 2012, and references therein), backflow, or jet activity interruptions (e.g. Schoenmakers et al. 2000). In some cases the jet-shell interaction model, which does not require a spin-flip or axis reorientation, has been proposed (Gopal-Krishna et al. 2012).

Radio sources that are Z- or X-shaped can be probes of binary black-hole systems in the galaxy, as a product of a galaxy merger. Gopal-Krishna et al. (2003) suggest that Z-shaped radio sources are at early stages of interaction with a dense environment, which was the result of the concentration of gas at a distance of ~10 kpc from the nucleus due to the galaxy merger. This interaction with the gas causes the jets to bend symmetrically when expelled from the source. The only observationally confirmed example of a binary black-hole galaxy system is the study of Rodriguez et al. (2006) in the radio galaxy 0402+379, with a projected separation between the black holes of 7.3 pc. X-shaped sources are assumed to be later stages of that interaction (Gopal-Krishna et al. 2003). A striking example in the multi-component sources is 10933, where we see this Z-shaped symmetric radio structure close to the nucleus (see Figs. D.3 and D.7).

To identify possible signatures of binary black-hole systems that give rise to this double-double radio structure, we cross-matched these sources with the 1.4 GHz VLBA data available for the COSMOS field (Herrera Ruiz et al. 2017).

We find five matches between X-shaped 3 GHz objects and VLBA data: 10909, 10914, 10918, 10919, 10933 and 10958. The observations can be seen in Fig. D.3. We also report the core flux densities from VLBA in Table A.1. In all five sources the 1.4 GHz VLBA core is offset from the 3 GHz VLA core, by about 0.04 arcsec, which is not significant; it is within the uncertainty of the astrometry in the 3 GHz mosaic.

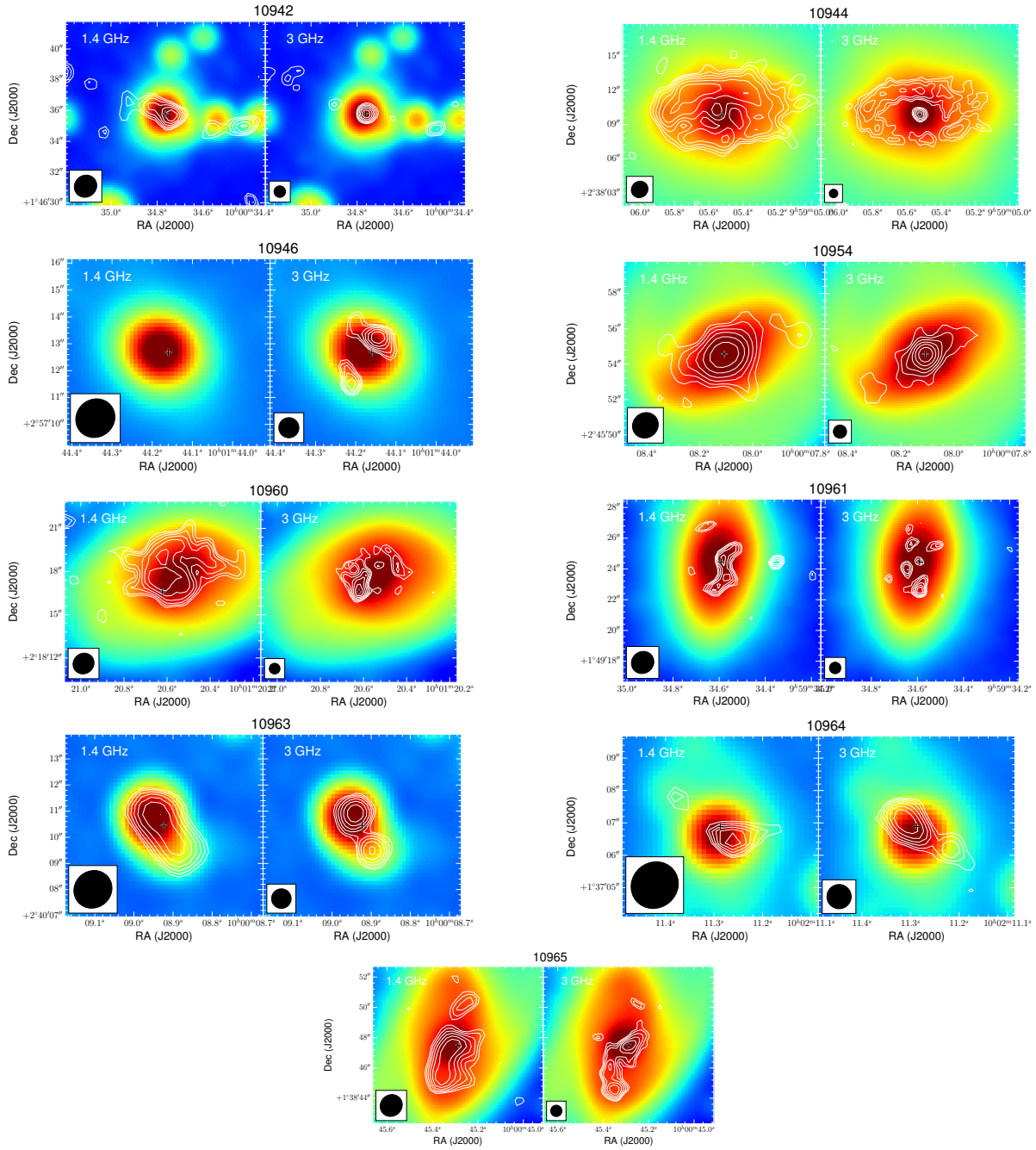

Fig. D.5. The nine star-forming-galaxies in our multi-component radio sample at 3 GHz, including uncertain object (marked as SFG* in Table A.1). The latter have been placed in this class as they are lacking radio excess (see Sect. 3.1). Images are described in Fig. D.7.

As seen in Fig. D.3, the radio cores are resolved and show some slight extended features (e.g. 10933). Source 10909 presents two strong emission peaks at VLBA separated by 0.05 arcsec. These lie on top of the fringes in the image, thus we refrain from making a strong statement about a double core. Source 10914, at $z_{\rm phot}$ = 1.437, displays a feature on the south-west of the core, but this could be due to band-width smearing, and the orientation of the jet is perpendicular to the direction of the 3 GHz emission.

D.1.4. Bent-tail multi-component AGN

In this section we present objects that show bending in their radio structure and in particular in the outer jets, in contrast to WAT sources that show bends on both jets close to the central galaxy. We identify three such objects (10917, 10947, and 10966) in our sample of multi-component radio sources (see Fig. D.4). We note that these are not all the bent radio sources at 3 GHz VLA-COSMOS, as there are also single-component bent sources not included in the multi-component sample.

Source 10917 displays a core and single lobe to the north and a faint blob to the south, which was included in the estimate of the flux of this object. Its lobe-like structure to the north, is bent probably due to interaction with the surrounding environment.

Source 10947 displays a core and single lobe to the west and a faint blob to the east, which was included in the flux of this object. Its structure looks quite different though from the 1.4 GHz analogue, where the bend on the west jet is not so pronounced.

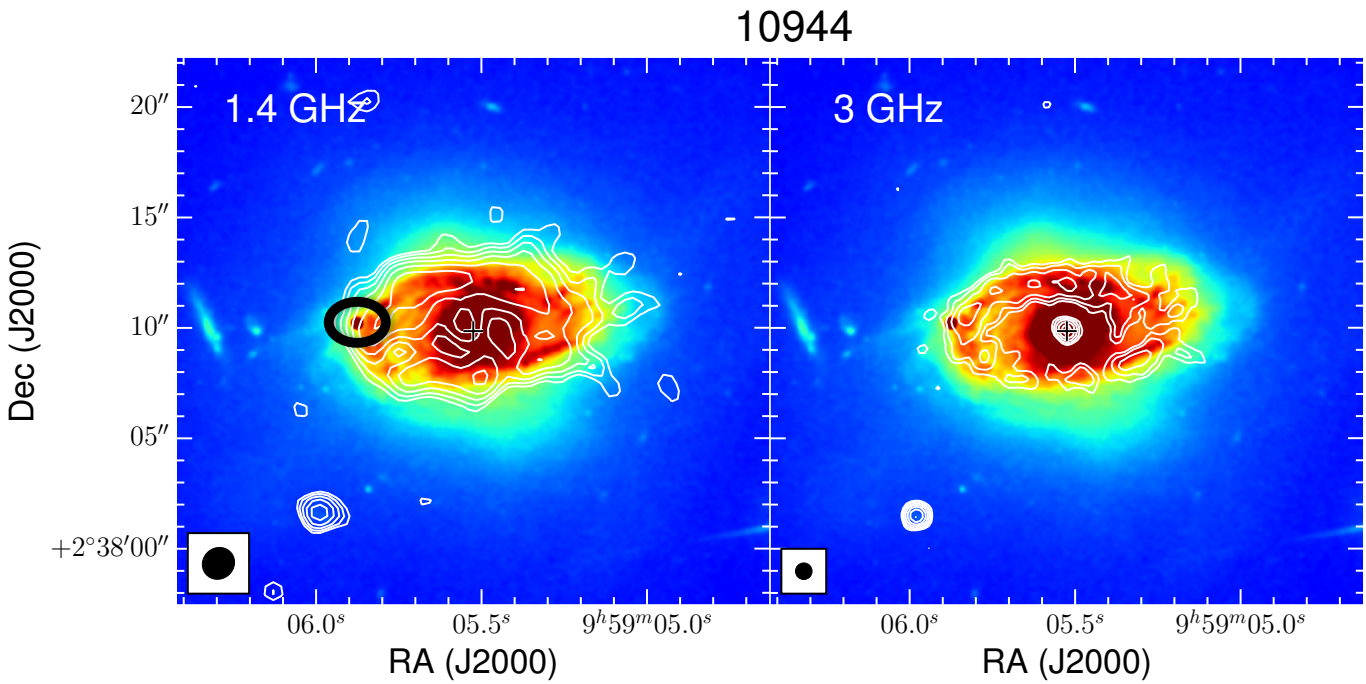

Fig. D.6. Source 10944 radio contours at 1.4 GHz (*left*) and 3 GHz (*right*) overlaid on the HST map (colour scale). The contours start at the 3σ level and rise logarithmically. The HST map is from Koekemoer et al. (2007). The black circle marks the knot discussed in the text.

Source 10966 is an example of a bent outer-jet. It exhibits bending towards the edge of both its jets, suggesting interaction with the ICM at distances far from the core of the radio source.

D.1.5. Symmetric multi-component AGN

This section lists the multi-component AGN that their lobes or jets form a 180° angle to each other. We classify these sources as symmetric multi-component AGN. We identify 26 such objects within the multi-component sample: 10901, 10902, 10904, 10905, 10906, 10907, 10908, 10911, 10916, 10920, 10921, 10922, 10923, 10925, 10926, 10928, 10930, 10932, 10934, 10936, 10937, 10938, 10948, 10951, 10953 and 10959. These can be found in Fig. D.7. All of these display two lobes or jets. The exception is 10905, where the east lobe is very diffuse. Similarly, 10911 has a well-defined north lobe but the south lobe is very diffuse at 3 GHz. Source 10937 is the smallest double source in our sample, with largest angular size of ~3 arcsec. Finally, in four sources both lobes are diffuse (10907, 10921, 10948 and 10951).

D.2. Multi-component SFGs

Our classification yields nine SFGs amongst the multi-component objects at 3 GHz VLA-COSMOS. These are presented in Fig. D.5, and the most striking case that shows a radio ring, 10944, is discussed in Appendix D.2.1. The rest of the objects show star-forming regions associated with the galaxy disk (shown in the infrared in the stacked Ultra-VISTA map). Below we give a brief description of the radio structure of the SFGs in our sample.

Source 10942 is classified as SFG based on the absence of radio excess (see Sect. 3.1). Multi-wavelength AGN diagnostics also suggest this is a SFG (from the publicly available counterpart catalogue of Smolčić et al. 2017b; see also Table 1). The map shows several radio blobs at 3 GHz, the strongest of which is coincides spatially with the galaxy in the infrared.

Source 10946 is classified as an SFG due to its radio structure at 3 GHz. There are no indications of a radio jet. The source is composed of two radio blobs at 3 GHz which lie on the galaxy disc. It lies outside the 1.4 GHz coverage of the COSMOS field.

Source 10954 is classified as star-forming galaxy due to the radio structure at 3 GHz, which has two radio blobs (one larger and one smaller) associated with the disk of the galaxy seen in the Ultra-VISTA map.

Source 10960 displays several blobs of different size and has a ring-like radio structure at 3 GHz. This is why it is classified as an SFG. At 1.4 GHz it is a single-component complex source.

Source 10961 is composed of several small approximately beam-sized blobs at 3 GHz, some larger some smaller, which coincide spatially with the disk of the infrared galaxy seen in the Ultra-VISTA map. This is why it is classified as an SFG. The 1.4 GHz map shows an S-shaped source and several smaller ones.

Source 10963 is a double source associated with the disk-of the infrared galaxy shown in Fig. 6. This initially was in the uncertain class, but we classify it as SFG due to the lack of radio excess (see Sect. 3.1).

Source 10964 is a double source at 3 GHz, with radio structure that is different from the one at 1.4 GHz. We classify this as an SFG due to the lack of radio excess (see Sect. 3.1). It is also SFG based on the SED fit (see Table 1).

10965 displays a large twisted blob at 3 GHz, which follows the spiral arm of the galaxy shown in infrared in Fig. D.5, and also has several smaller blobs associated with the galaxy disc. This is why we classify it as an SFG.

D.2.1. The “eye” of COSMOS: A star-forming radio galaxy ring

Based on the 3 GHz radio map (Fig. D.6), 10944 is a star-forming radio ring with a compact radio core in the centre, associated with the nucleus of the galaxy. This ring-like radio synchrotron emission follows well the spiral arms of this face-on

galaxy, as seen in the overlay image of the radio and Hubble space telescope (HST) i-band image (Koekemoer et al. 2007). From the HST image we classify this particular galaxy as a polar-ring galaxy (e.g. Moiseev et al. 2011), because it exhibits an elongation along in the NW-SE direction, almost perpendicular to the disc. Polar-ring galaxies are the result of galaxy mergers, and this would indicate that 10944 is the result of a galaxy merger. This the only object in COSMOS that shows a radio ring and a compact radio core.

The unprecedented high resolution of 0.75 arcsec of the 3 GHz VLA-COSMOS data has revealed the sub-structure in the ring, which is not seen at 1.4 GHz. Besides the ring, we also see a small unresolved core associated with the centre of the galaxy. To investigate whether this is due to star formation or an AGN, we cross-matched it to the VLBA data available for the COSMOS field from Herrera Ruiz et al. (2017), but we found no match: this source has been observed but not detected by VLBA (Herrera Ruiz priv. comm.). The host galaxy is an SF galaxy at low redshift, $z_{\rm spec} = 0.07905$, with no signs of AGN at any observed wavelengths, and it does not display any radio excess over the star formation rate. Our multi-wavelength AGN diagnostics do not show any evidence for the existence of an AGN. It is not a mid-IR AGN or an X-ray AGN and is classified as an SFG (Smolčić et al. 2017b).

Only 4% of the flux is located in the "core", while the rest is in the ring structure. It has a $\mathrm{SFR_{IR}} = 4.9\,M_{\odot}\,\mathrm{yr}^{-1}$ and a stellar mass of $2.8 \times 10^{11}\,M_{\odot}$ and falls just below the 1σ dispersion of the main sequence for star-forming galaxies (e.g. Whitaker et al. 2012) at the redshift of the source. It is a sub-luminous infrared galaxy (sub-LIRG) with total infrared luminosity $L_{\rm IR} = 4.9 \times 10^{10}\,L_{\odot}$.

The radio "core" emission at 3 GHz is barely resolved at 3 GHz, giving an upper limit for the size of the radio emitting area at 1.12 kpc (full width half maximum – FWHM). We also note that the peak "core" emission is slightly offset at 1.4 GHz from that at 3 GHz, by 0.57 arcsec. This could be attributed to differences in the beam and pixel size between the two maps, or could simply be an effect of noise.

Given that there is no indication of an AGN from the multi-wavelength AGN diagnostics available for COSMOS, we conclude that this is a circum-nuclear star-forming region close to the nucleus of this galaxy and the radio emission is not a result of an AGN. If indeed there were a low-luminosity AGN, this would be Compton-thick and heavily obscured by dust surrounding the nuclear region.

The bright knot at the eastern part of the ring (marked with a black circle) can be seen in the 1.4 GHz, 3 GHz and HST maps in Fig. D.6 but it does not spatially coincide, and it lies at a distance of ~7 kpc from the 3 GHz "core". The distance between the HST and 3 GHz local peak flux density is 0.9 arcsec and between the HST and 1.4 GHz local flux density 3 arcsec. Probably this is a star-forming region associated with the spiral arm of the galaxy. Finally, the radio ring has a radius of ~6.5 kpc (major axis) and ~2.8 kpc (minor axis).

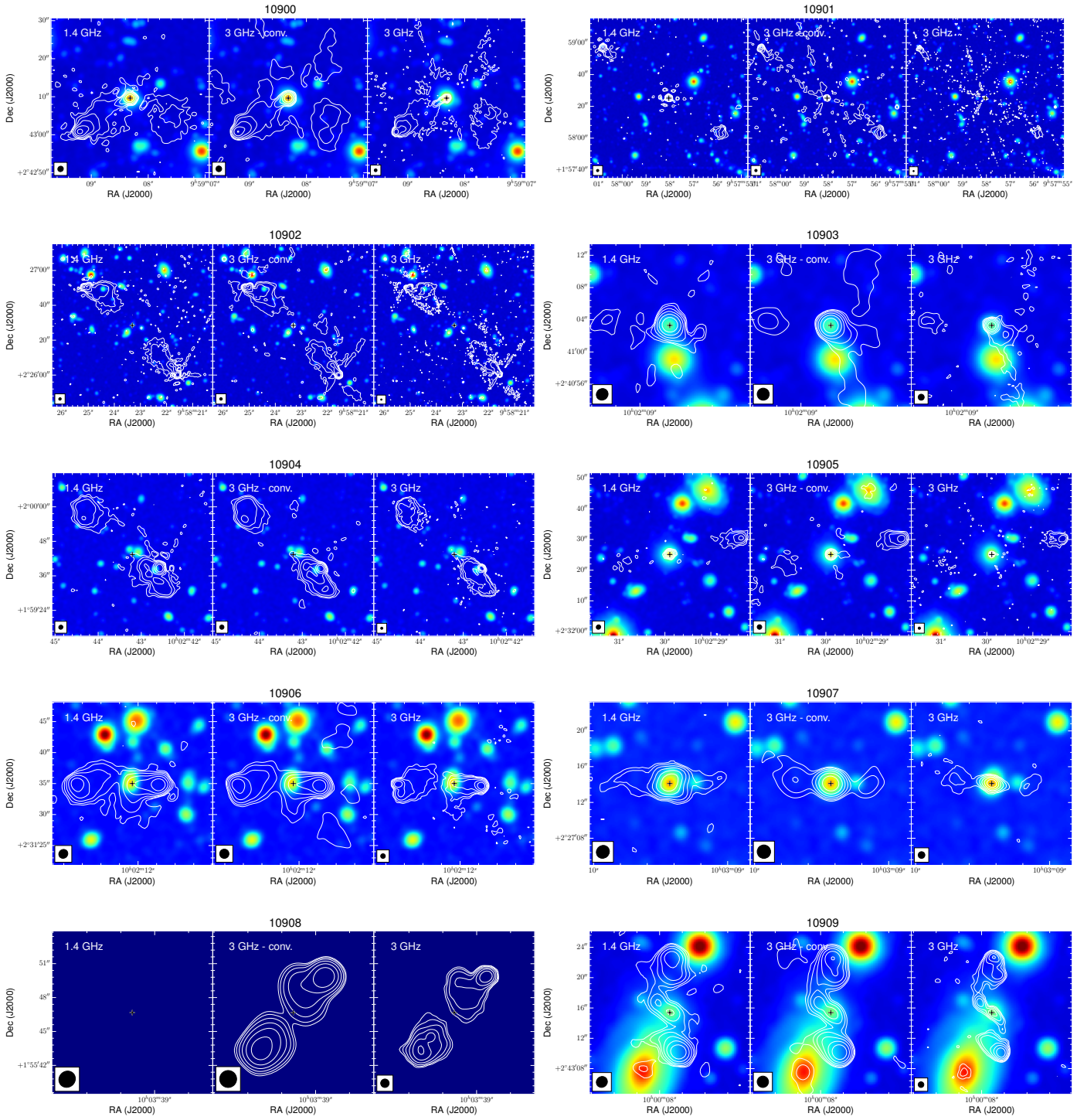

Fig. D.7. Set of VLA 1.4 GHz and 3 GHz VLA-COSMOS stamps for the multi-component objects. For each object we give the 1.4 GHz map (*left*), the 3 GHz map at the original resolution of 0.75 arcsec (*right*), and the convolved 3 GHz map at 1.5 arcsec resolution (*middle*), to match the one at 1.4 GHz. The contour levels are equally spaced on a log scale, where the lowest is set at 3σ and the highest at the maximum peak flux density of the radio structure, and are overlaid on the UltraVISTA stacked image (see Sect. 2). The 1.4- and 3 GHz beams are shown on the bottom left. Objects without a colour background are located in masked areas in the UltraVISTA coverage. Some objects also lack 1.4 GHz contours, as they lie outside the 1.4 GHz coverage.

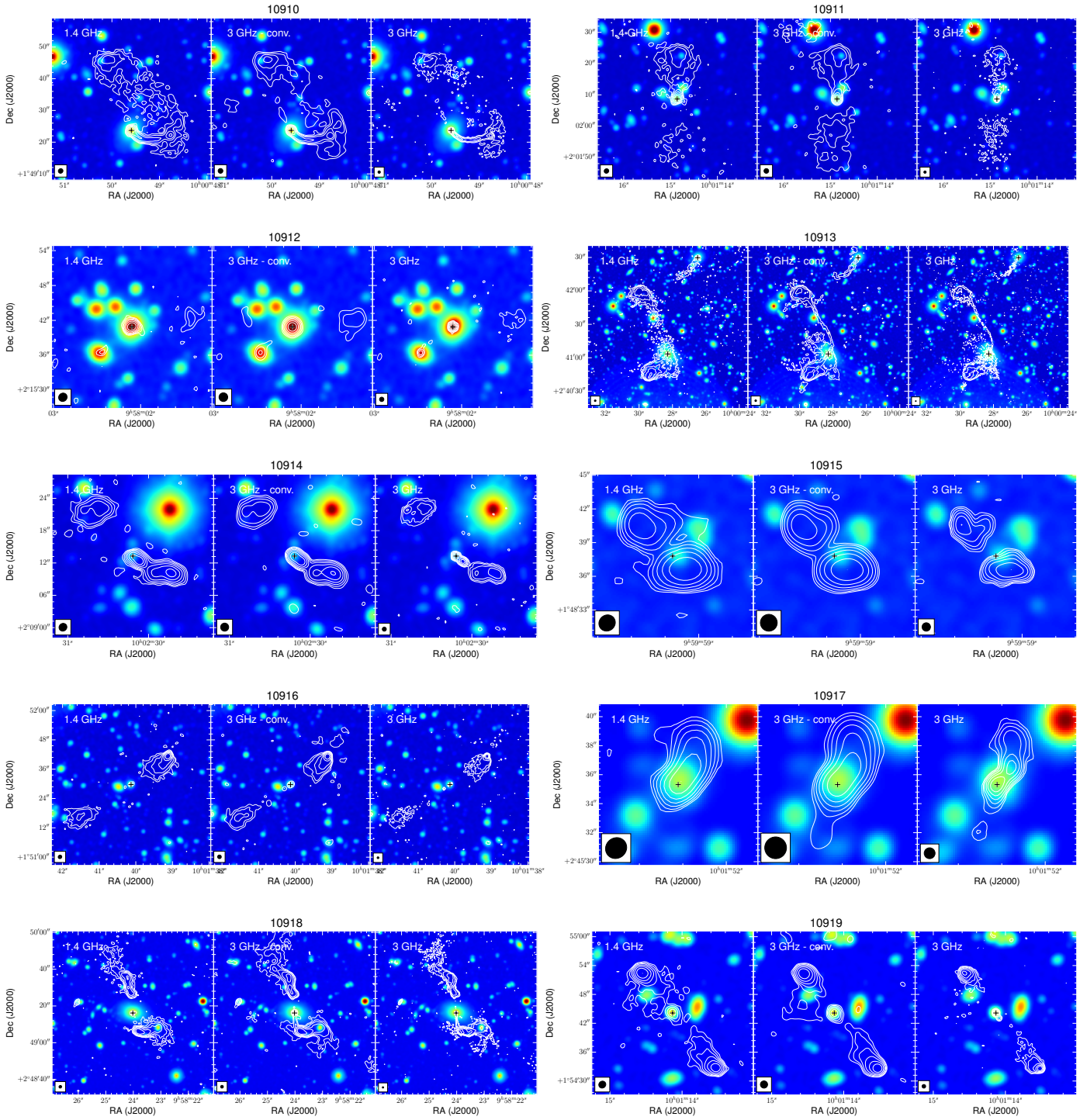

Fig. D.7. continued.

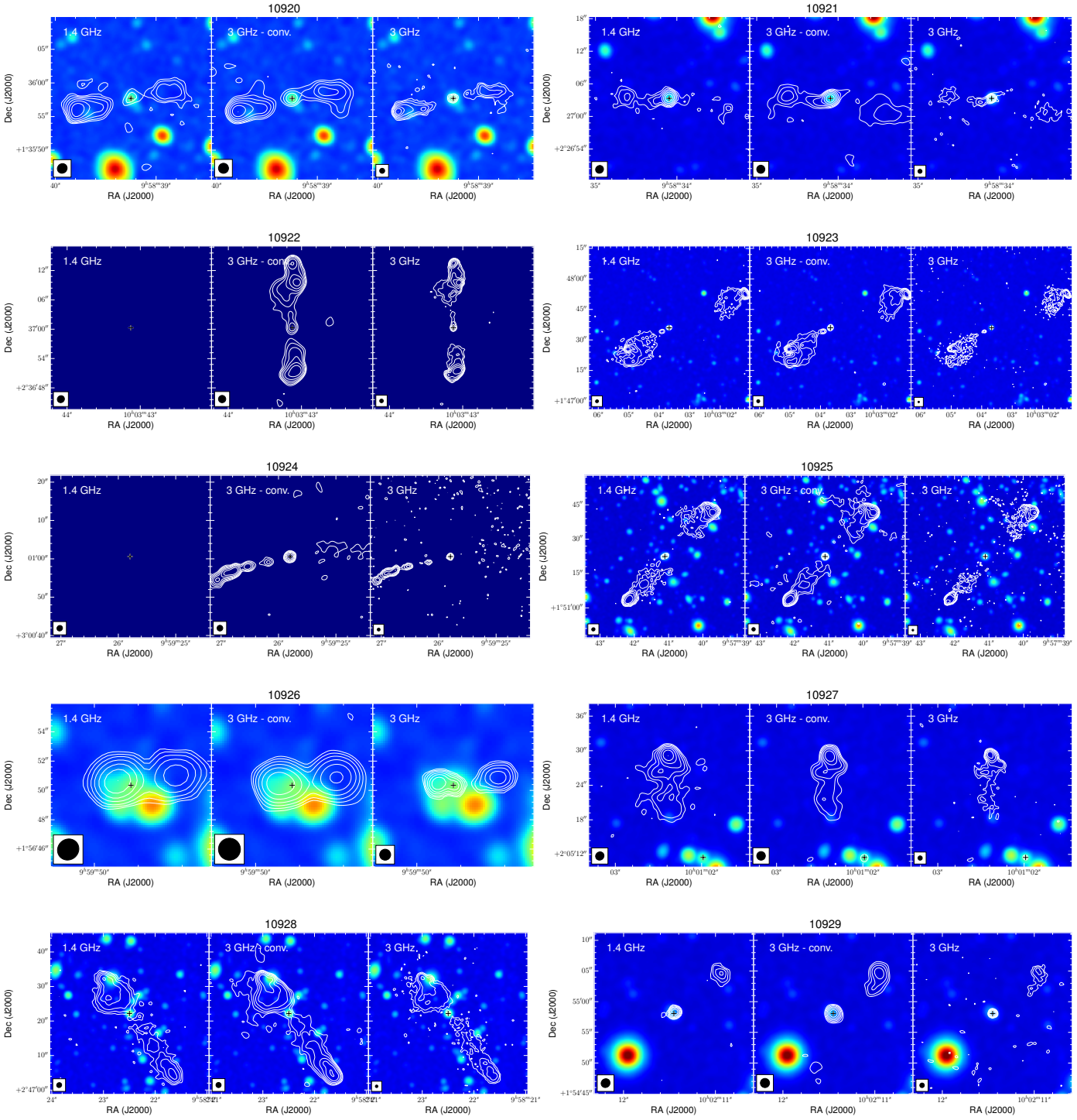

Fig. D.7. continued.

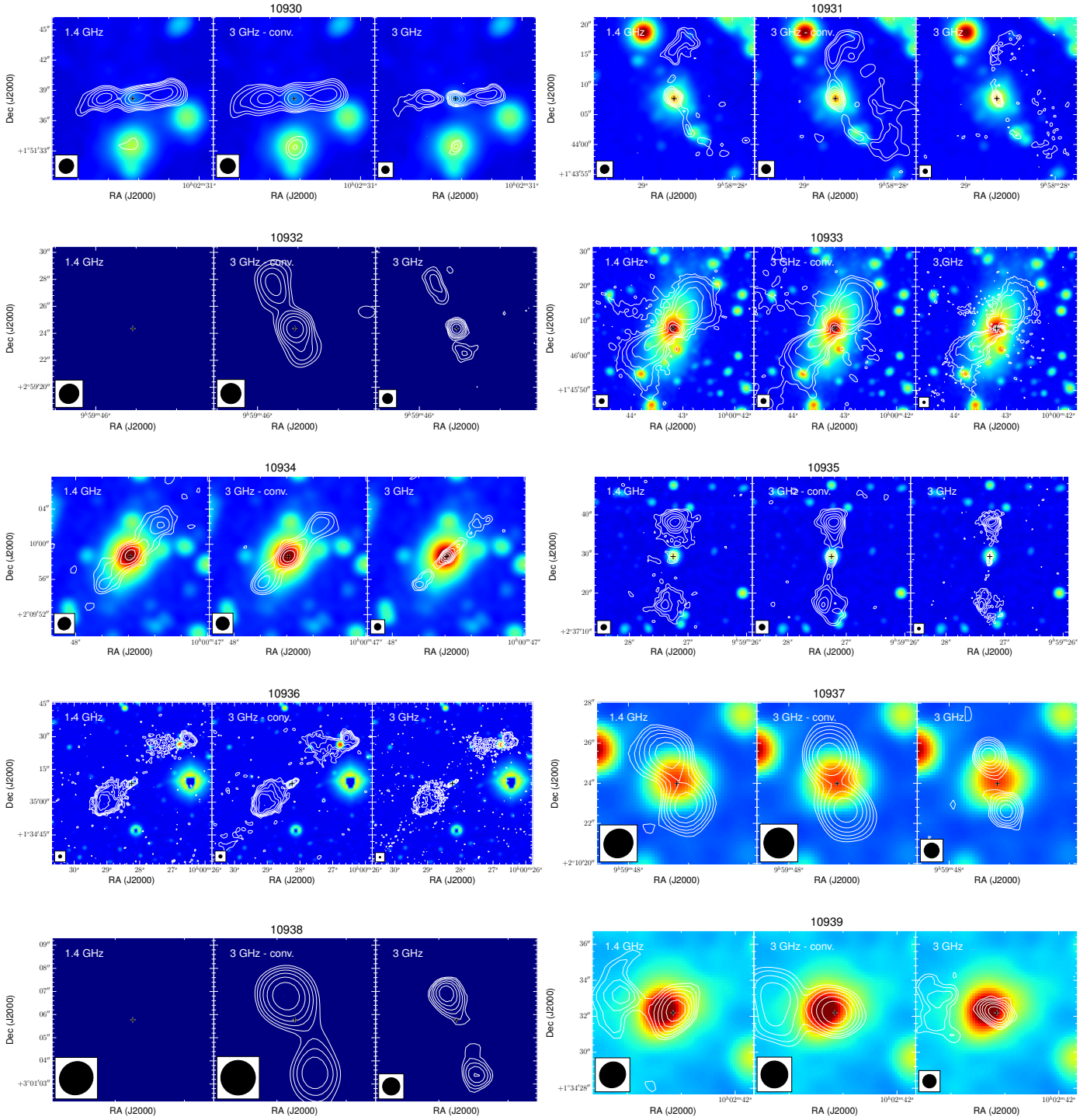

Fig. D.7. continued.

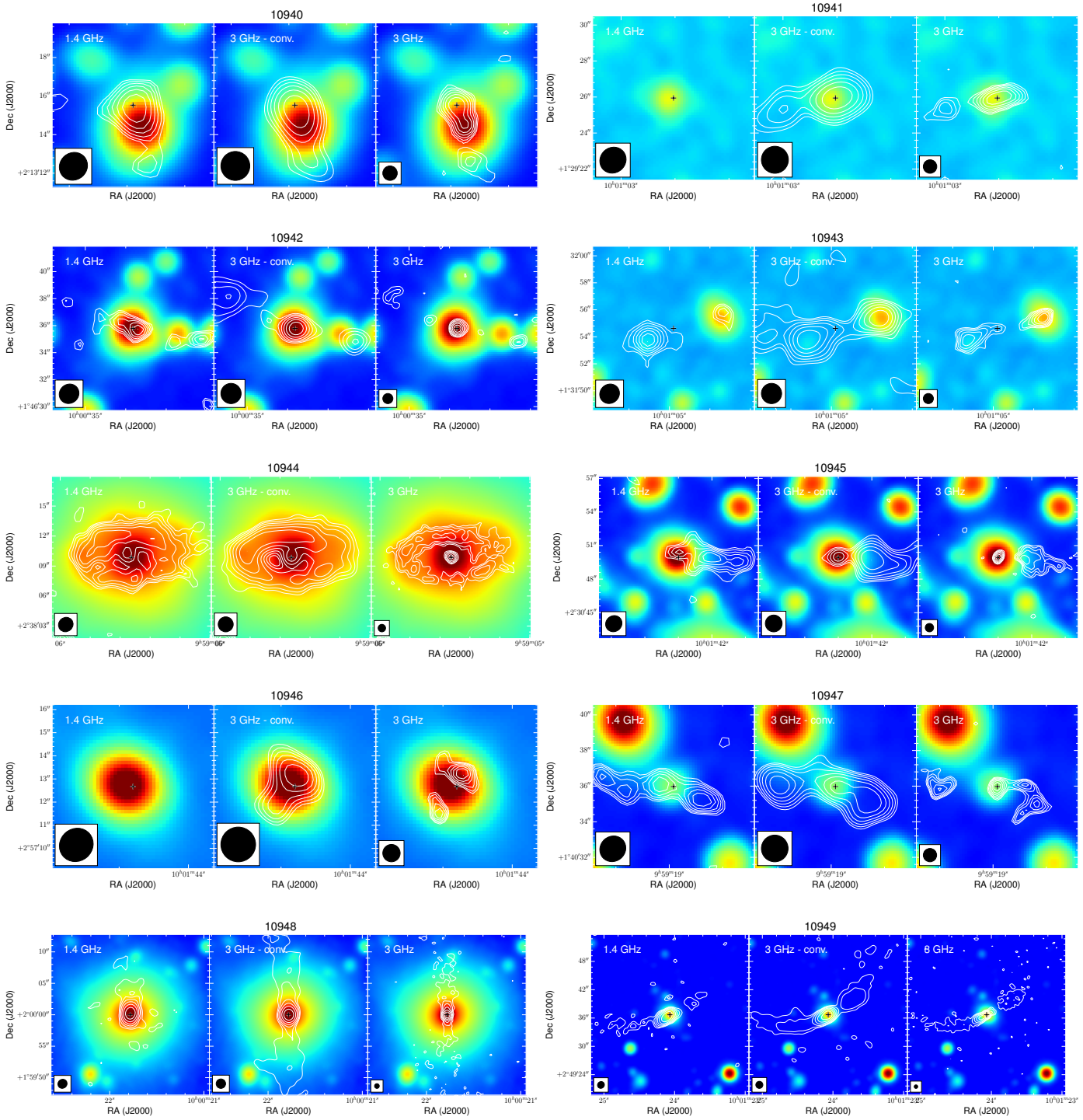

Fig. D.7. continued.

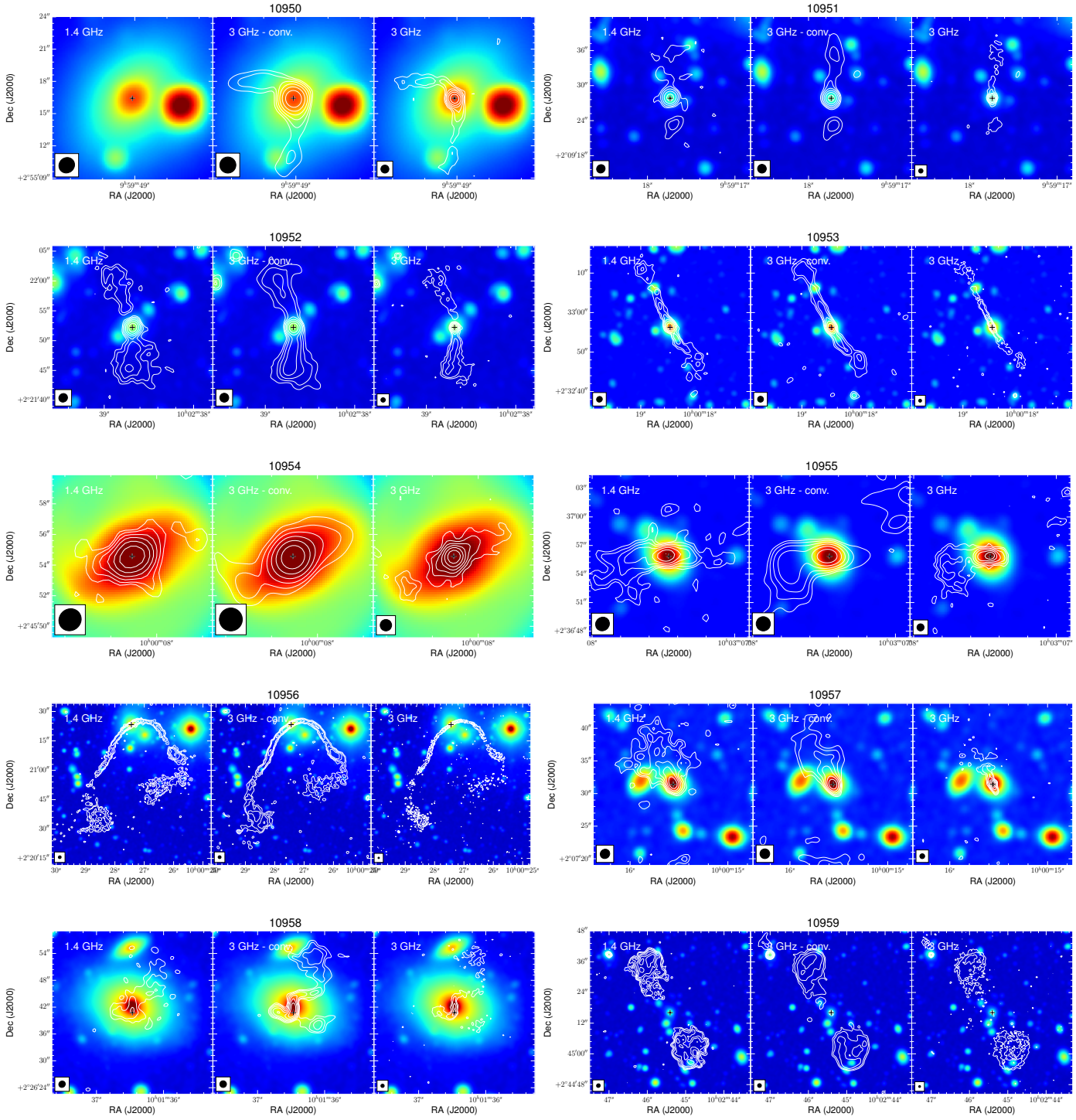

Fig. D.7. continued.

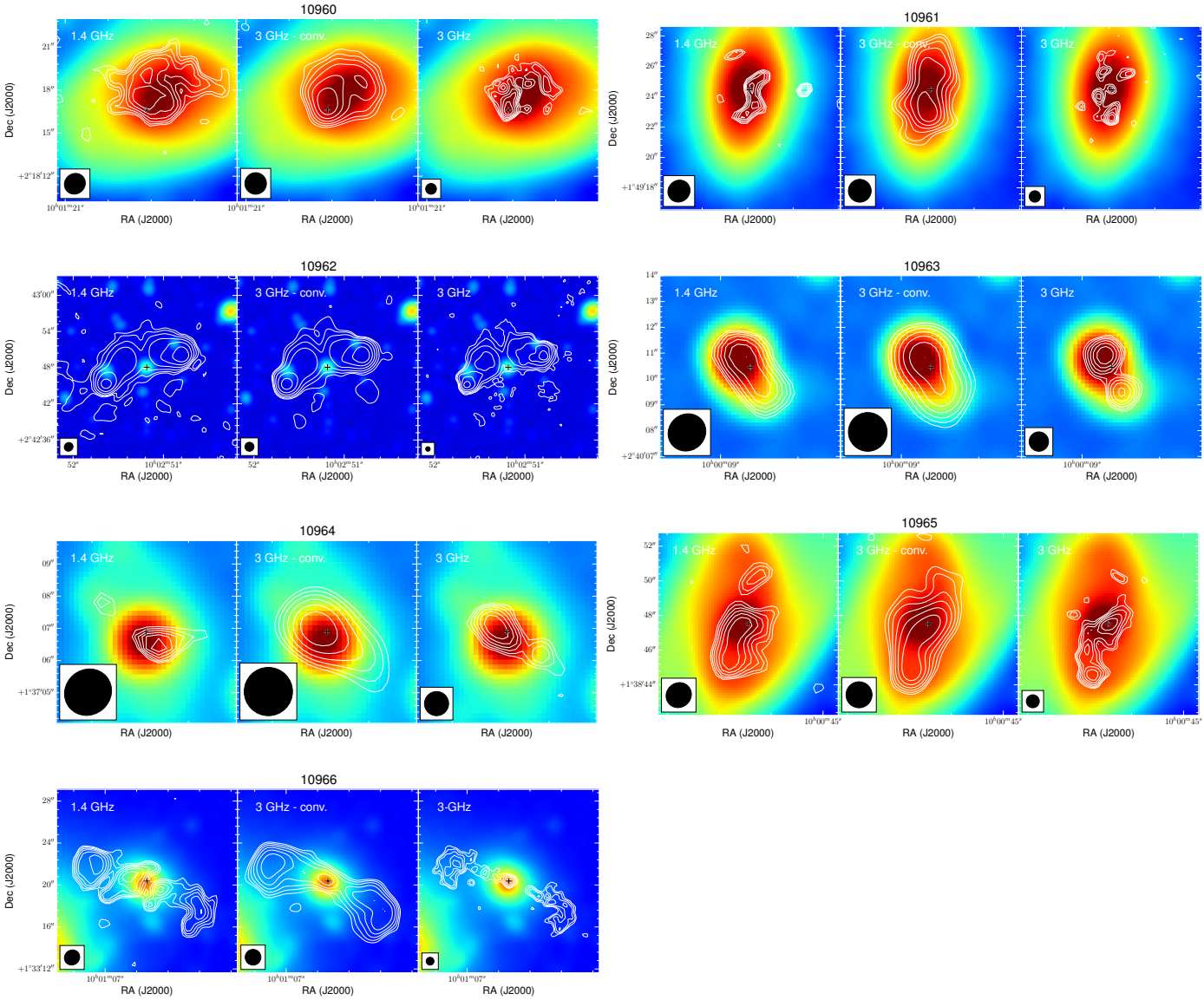

Fig. D.7. continued.